JGR Planets

RESEARCH ARTICLE
10.1029/2018JE005666

Special Section:
Ice on Ceres

Fluidized Appearing Ejecta on Ceres: Implications for the Mechanical Properties, Frictional Properties, and Composition of its Shallow Subsurface

Kynan H. G. Hughson[1], C. T. Russell[1], B. E. Schmidt[2], H. T. Chilton[2], H. G. Sizemore[3], P. M. Schenk[4], and C. A. Raymond[5]

[1]Department of Earth, Planetary, and Space Sciences, University of California, Los Angeles, CA, USA, [2]School of Earth and Atmospheric Sciences, Georgia Institute of Technology, Atlanta, GA, USA, [3]Planetary Science Institute, Tucson, AZ, USA, [4]Lunar and Planetary Institute, Houston, TX, USA, [5]Jet Propulsion Laboratory, Pasadena, CA, USA

Key Points:
- We identify 30 examples of fluidized appearing ejecta on Ceres
- Cerean fluidized appearing ejecta are divided into two morphological populations: channelized and cuspate/lobate
- The mobility of fluidized appearing ejecta on Ceres suggest that it has a weak low-friction surface consistent with abundant shallow ground ice

Supporting Information:
- Supporting Information S1
- Figure S1
- Figure S2
- Figure S3
- Figure S4
- Figure S5
- Figure S6
- Figure S7
- Figure S8
- Figure S9
- Figure S10
- Figure S11
- Figure S12
- Figure S13
- Figure S14
- Figure S15
- Figure S16
- Figure S17
- Figure S18
- Figure S19
- Figure S20
- Figure S21
- Figure S22
- Figure S23
- Figure S24
- Figure S25
- Figure S26
- Figure S27
- Figure S28
- Data Set S1
- Data Set S2

Correspondence to:
K. H. G. Hughson,
p151c@ucla.edu

Citation:
Hughson, K. H. G., Russell, C. T., Schmidt, B. E., Chilton, H. T., Sizemore, H., Schenk, P. M., & Raymond, C. A. (2019). Fluidized appearing ejecta on

Abstract Several ejecta deposits on Ceres display morphological characteristics not commonly associated with dry ballistic emplacement. We characterized 30 examples of fluidized appearing ejecta (FAE) on Ceres and identified two distinct morphological populations: cuspate/lobate FAE and channelized FAE. The cuspate/lobate FAE typically display one or more of the following characteristics: well-defined margins, a sheeted or layered appearance, arcuate or cuspate terminal lobes, and occasional mass concentrations at their distal margins. The channelized FAE typically display a morphology dominated by topographically focused channelized flows and arcuate terminal lobes but lack the well-defined margins common among their cuspate/lobate counterparts. Although Cerean FAE are holistically distinct from rampart/layered ejecta craters on Mars, Ganymede, and other icy solar system objects, many of their aforementioned morphological characteristics are commonly found among these other examples of fluidized ejecta. The formation of Martian and icy satellite fluidized ejecta has been widely attributed to the mobilization of near-surface volatiles, namely, water ice. The documented Cerean FAE are observed between absolute latitudes of 70°, with a slight enrichment in the midlatitudes of the southern hemisphere. We test the hypothesis that the morphologies and mobilities of Cerean FAE can be explained via impacting into a low-cohesion ice-silicate target material, followed by material sliding on a low-friction partially icy substrate. We do this by comparing the observed Cerean FAE to a kinematic-dynamic sliding ejecta emplacement model. We find that a mechanically weak, H_2O-rich near-surface layer is consistent with the range of ejecta mobilities and morphologies observed in this investigation.

Plain Language Summary In March 2015, National Aeronautics and Space Administration's Dawn spacecraft began orbiting the dwarf planet Ceres, the largest object in the main asteroid belt between Mars and Jupiter. Pre-Dawn research demonstrated that a major volume fraction of Ceres may be composed of water ice, but the amount and distribution of that ice in the upper layer of the dwarf planet is still poorly understood. When Dawn began acquiring data, it observed a small, but significant, number of craters whose ejecta exhibited morphological signs of fluidization, which were similar to fluidized ejecta observed on Mars, Ganymede, Charon, and other icy worlds. We mapped and characterized all the instances of these fluidized appearing ejecta, which are observed between absolute latitudes of 70°, in order to establish any geographical trends and relationships. We then tested the hypothesis that the morphologies and spatial extents of Cerean fluidized appearing ejecta can be explained via impacting into low-cohesion ice-rock target materials, followed by material sliding on low-friction partially icy substrates. We did this by comparing the observed ejecta runout distances to a physics-based ejecta emplacement model. We found that an ice-rich near-surface layer on Ceres is consistent with the range of ejecta runout lengths and morphologies observed.

1. Introduction

After completing a thorough investigation of the asteroid (4) Vesta, NASA's Dawn mission (Russell et al., 2016) became the first spacecraft to enter orbit around two separate extraterrestrial objects in March of 2015 when it began making detailed scientific observations of the dwarf planet (1) Ceres. Dawn observed that a small but significant number of Cerean craters exhibited ejecta morphologies that reflect a significant

Ceres: Implications for the mechanical properties, frictional properties, and composition of its shallow subsurface. *Journal of Geophysical Research: Planets*, *124*, 1819–1839. https://doi.org/10.1029/2018JE005666

Received 1 MAY 2018
Accepted 20 FEB 2019
Accepted article online 27 FEB 2019
Published online 12 JUL 2019

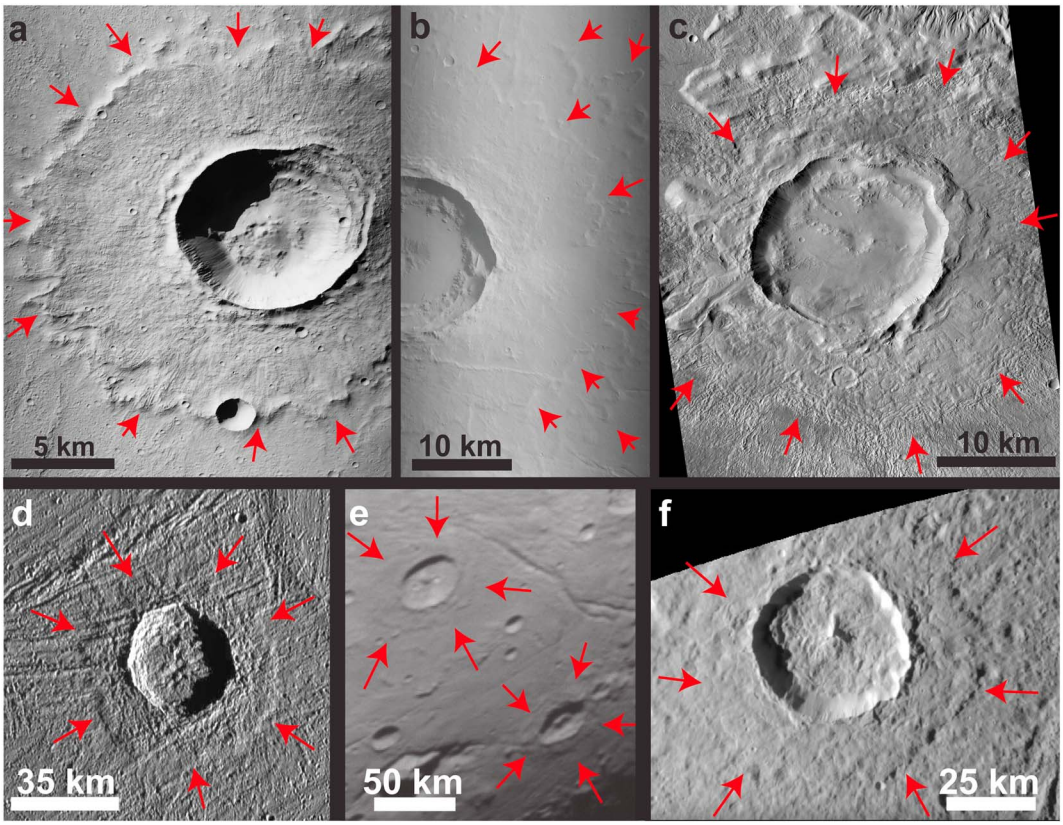

Figure 1. Examples of various types of fluidized ejecta throughout the solar system: (a) single-layer ejecta crater on Mars (25.9°S, 152.4°E; Mars Reconnaissance Orbiter's Context Camera (CTX) image, Planetary Data System [PDS] ID P17_007554_2154); (b) multiple-layered ejecta on Mars (22°N, 146°E; CTX image, PDS ID P07_003624_2041); (c) double-layer ejecta crater on Mars (30.4°N, −86.3°E; CTX image, PDS ID D22_035780_2101); (d) Achelous crater on Ganymede exhibiting a rampart morphology (61.8°N, 11.7°W; Cassini's Solid-State Imaging instrument image mosaic courtesy of Paul Schenk); (e) abruptly terminating ejecta on Charon, the identified crater in the top left is Spock (14.7°N, 25.7°E), the identified crater in the bottom right is unnamed (New Horizons' Long Range Reconnaissance Imager image, PDS ID lor_0299171413_0x636_sci); (f) Sagaris crater on Dione exhibiting abruptly terminating ejecta (25°S, 79°E; ISS image mosaic courtesy of Paul Schenk). Major terminal ejecta lobes and flow fronts are indicated by the red arrows.

degree of fluidization and suggest that they were emplaced as ground-hugging flows (Hughson et al., 2018; Schmidt et al., 2017). In contrast with most lunar and Mercurian ejecta, which are predominantly emplaced by ballistic sedimentation and have limited runout distances (Barnouin et al., 2012; Runyon & Barnouin, 2018; Shoemaker, 1962), these Cerean fluidized appearing ejecta (FAE) commonly have one or many of the following characteristics: well-defined (i.e., nongradational/abruptly terminating) margins, a sheeted or layered appearance, arcuate or cuspate terminal lobes, longitudinal grooves, channelized flows, and occasional mass concentrations at their distal margins. Although Cerean FAE have no holistically perfect analogues on other solar system objects, the aforementioned morphological characteristics are also found among layered ejecta, abruptly terminating ejecta, and rampart craters on Mars, Ganymede, Europa, Dione, and Charon (e.g., Boyce & Mouginis-Mark, 2006; Boyce et al., 2010; Carr et al., 1977; Gault & Greeley, 1978; Horner & Greeley, 1982; Jaumann et al., 2009; Li et al., 2015; Mouginis-Mark, 1979, 1981; Robbins et al., 2018; Schenk, 2010; Schultz & Gault, 1979; Woronow, 1981; Figure 1). There is currently no scientific consensus on the mechanisms of fluidization for Martian and Ganymedean layered ejecta; however, a plurality of investigators have interpreted the characteristics of these deposits to be due predominantly to the presence of volatiles, particularly water ice, in the upper layer of the target bodies (e.g., Barlow, 2005; Barlow & Bradley, 1990; Barlow & Perez, 2003; Boyce et al., 2010; Boyce & Mouginis-Mark, 2006; Carr et al., 1977; Mouginis-Mark, 1981, 1987; Osinski, 2006; Senft & Stewart, 2008; Stewart et al., 2001; Weiss & Head, 2013, 2014, 2018). Other proposed factors that may contribute to the fluidized appearance of these deposits are ejecta-atmosphere interactions (e.g., Schultz, 1992; Schultz & Gault, 1979;

Barnouin-Jha & Schultz, 1998; Barnouin-Jha et al., 1999a, 1999b; Barlow, 2005; Boyce & Mouginis-Mark, 2006; Boyce et al., 2010; Komatsu et al., 2007), base surges from the collapse of the main vertical ejecta column or near-rim ejecta (e.g., Barlow & Boyce, 2013; Boyce et al., 2012; Boyce & Mouginis-Mark, 2006), continuum fluid flow (e.g., Baloga et al., 2005; Barnouin-Jha et al., 2005; Mouginis-Mark & Baloga, 2006), and granular flow (e.g., Wada & Barnouin-Jha, 2006).

Ceres' low bulk density of 2162 ± 8 kg/m^3 (Park et al., 2016) has long been suggestive of a composition that is rich in water ice, hydrated materials, and/or organic compounds (Castillo-Rogez & McCord, 2010; McCord & Sotin, 2005; Russell et al., 2016; Thomas et al., 2005; Zolotov, 2009). The interpretation that Ceres' uppermost layer is rich in water ice is further strengthened by additional spectral observations of H_2O ice absorption features at geographically diverse locations on Ceres in spite of its thermodynamic instability (Combe et al., 2016, 2019), nuclear spectroscopy results that predict a thinly armored surface ice table at absolute latitudes greater than ~40° (Prettyman et al., 2017), and gravitational/topographic studies that predict ~25 vol.% ice in the upper ~40 km of Ceres (Ermakov et al., 2017; Fu et al., 2017). Despite these observations, the distribution and concentration of water ice in the upper layer of Ceres is still poorly constrained at the scale of several tens of kilometers and finer.

Layered ejecta craters on Mars and FAE on Ceres display significant variation in their ejecta mobility (EM) ratios, which is defined as the ratio of a continuous FAE facies' mean distal radius from the crater rim over the observed crater rim radius (R_e/R_f; e.g., Barlow, 2005; Barlow & Pollak, 2002; Carr et al., 1977; Mouginis-Mark, 1979; Weiss & Head, 2014). In the case of Mars, these variations in EM values have variously been attributed to modulations in the abundance of near-surface volatiles (Barlow & Pollak, 2002; Gault & Greeley, 1978; Weiss & Head, 2014), variations in the distribution of volatiles in the target material (Costard, 1989), variations in the mechanical properties of the near-surface (Wada & Barnouin-Jha, 2006), and ejecta-atmosphere interactions (Schultz, 1992). The three former factors are of particular interest in the case of FAE on Ceres.

In this study we test the hypothesis that the morphologies and various EM values of Cerean FAE deposits can be explained via impacting into a low-cohesion ice-silicate target material, and material sliding on a low-friction substrate. The aforementioned factors are directly controlled by the abundance and distribution of ground ice in the region immediately proximal to the impact. We do this by identifying and characterizing morphologically distinct Cerean FAE through geologic mapping, analyzing their geographic distribution, measuring their EM values, and by comparing these values to a hybrid kinematic-dynamic sliding ejecta emplacement model moderately similar to the kinematic model developed by Weiss and Head (2014) for applications on Mars.

2. Data Sets and Methods

2.1. Photographic Data

The data used in the identification and quantification of Cerean FAE were entirely photographic and stereophotogrammetric in nature. The analyzed images were collected during Dawn's High Altitude Mapping Orbit (HAMO: 1,470 km altitude) and Low Altitude Mapping Orbit (LAMO: 375-km altitude) by the spacecraft's framing camera (FC; Sierks et al., 2011). These clear and color filter FC data were acquired globally at ~140 and ~35 m/pixel, from the HAMO and LAMO mission phases, respectively. Globally acquired FC images taken from HAMO were used to generate the stereophotogrammetric digital terrain model (DTM) of Ceres (vertical accuracy ~10 m; Preusker et al., 2016). For details on the calibration of FC images see Schröder et al. (2013) and Schröder et al. (2014).

2.2. FAE Identification and Characterization Through Geomorphological Mapping

Previous global mapping campaigns by Buczkowski et al. (2016) and Schmidt et al. (2017) identified 18 landslide-like deposits that they termed “Type 3 flows”. Schmidt et al. (2017) interpreted these Type 3 flows as possible instances of fluidized ejecta mainly by virtue of their thin sheeted appearance and anomalously low drop-height-to-runout-length (H/L) ratios that display no correlation with average flow length. These low H/L values are analogous to having high runout efficiencies (e.g., Barnouin-Jha & Buczkowski, 2007; Runyon & Barnouin, 2018). Inspired by the results of Schmidt et al. (2017), we conducted a global geomorphologic mapping campaign expanding on their criteria to identify and characterize prominent instances of

FAE on Ceres. Specifically, we mapped ejecta facies that displayed at least one direct morphological indication of fluidization, namely, the presence of discrete cuspate or arcuate terminal lobes, a sheeted or multilayered appearance, abrupt or well-defined margins, superimposed longitudinal grooves, or topographically controlled channelized flow (i.e., ejecta that has been confined to areas of relatively low topography and/or been focused or deflected by topographic obstacles). Ejecta facies that did not display any of the aforementioned characteristics were interpreted as dry runout flows and not included in our mapping. Distinct occurrences of landslides within or coincident with FAE are discussed in Duarte et al. (2019) and may be formed during or after FAE emplacement.

In total, we identified 30 robust occurrences of FAE on Ceres that we interpreted as belonging to two separate morphological populations: a channelized FAE population and a cuspate/lobate population. The 11 identified channelized FAE display multiple prominent instances of topographic control (e.g., pooling in depressions, formation of numerous small channels in low lying regions, and being easily diverted around isolated instances of high standing terrain), occasional flow banding, and have thin sheeted appearances; they do not exhibit well-developed cuspate lobes, longitudinal grooves, or a multilayered appearance and have well-defined terminal margins only intermittently around their distal margins. The remaining 19 cuspate/lobate FAE display prominent cuspate or arcuate terminal lobes, a layered or multilayered appearance and have well-defined distal margins around the majority of their perimeter. These cuspate/lobate FAE also display occasional longitudinal grooves near the rims of their source craters, and mass concentrations near their distal margins. Typical examples of Cerean channelized and cuspate/lobate FAE, their mapped facies, and their local topography are shown in Figure 2 in the supporting information (similar renderings for all 30 identified Cerean FAE are given in supporting information Figures S1–S28). In general, Cerean FAE were found to be predominantly associated with morphologically fresh appearing impact craters. Specific morphological characteristics of cuspate/lobate and channelized Cerean FAE are displayed in Figures 3 and 4, respectively. This mapping analysis, as well as the global search campaign, was completed using ArcMap 10.3.

Once FAE were identified geomorphically, both their source crater radii and rim-to-terminus ejecta emplacement distances were quantified. Due to the fact that many of the examined craters did not exhibit radially symmetric geometries, we measured their radii as the length-weighted mean distance from their rims to the centroid of their mapped polygon (see Figure 2 for examples of mapped polygons). Likewise, we measured the rim-to-terminus ejecta emplacement distance as the length-weighted mean distance from the distal margin of the outermost mapped FAE facies to the centroid of its source crater, minus the mean radius of the source crater itself. Beyond using length-weighted mean crater radii, the effects of elliptical crater geometries on measured EM values are not considered. This simplification is justified due to the generally low observed ellipticity of FAE source craters (see supporting information Figures S1–S8). Although our geomorphic mapping, like all attempts at geologic mapping, suffers from a degree of subjectivity, the resultant values for FAE source crater radii, ejecta runout distance, and EM are fully self-consistent. We estimate that they suffer from no more than (±) a few percent errors.

Additionally, the spatial derivative of the HAMO stereophotogrammetric DTM was used to quantify the mean regional slopes radially away from the rims of FAE source craters. This exercise was completed in order to calibrate the measured EM values to a common slope gauge, so that the analysis of these values (albeit crudely) was independent of variations in the slope local to each instance of FAE. This was accomplished through the use of ArcMap's Zonal Statistics tool.

2.3. Geospatial Analysis and Distribution Modeling of FAE

On Mars, fluidized ejecta craters display distinct latitudinal distribution trends based on their specific morphology (Weiss & Head, 2014). It is likely that these distributions are controlled primarily by the availability of near-surface/surface ground ice and its stratigraphic locations (Barlow & Perez, 2003). If latitudinal trends exist in the distribution of FAE on Ceres they would most likely be caused by variations in the near-surface ground ice content (Schmidt et al., 2017) due to enhanced desiccation near the equator (Prettyman et al., 2017), and/or by decreased volatility of ice, clathrates, and hydrated salts in the very near surface at the poles due to the ~50-K decrease in the mean annual surface temperature relative to the equator (Hayne & Aharonson, 2015).

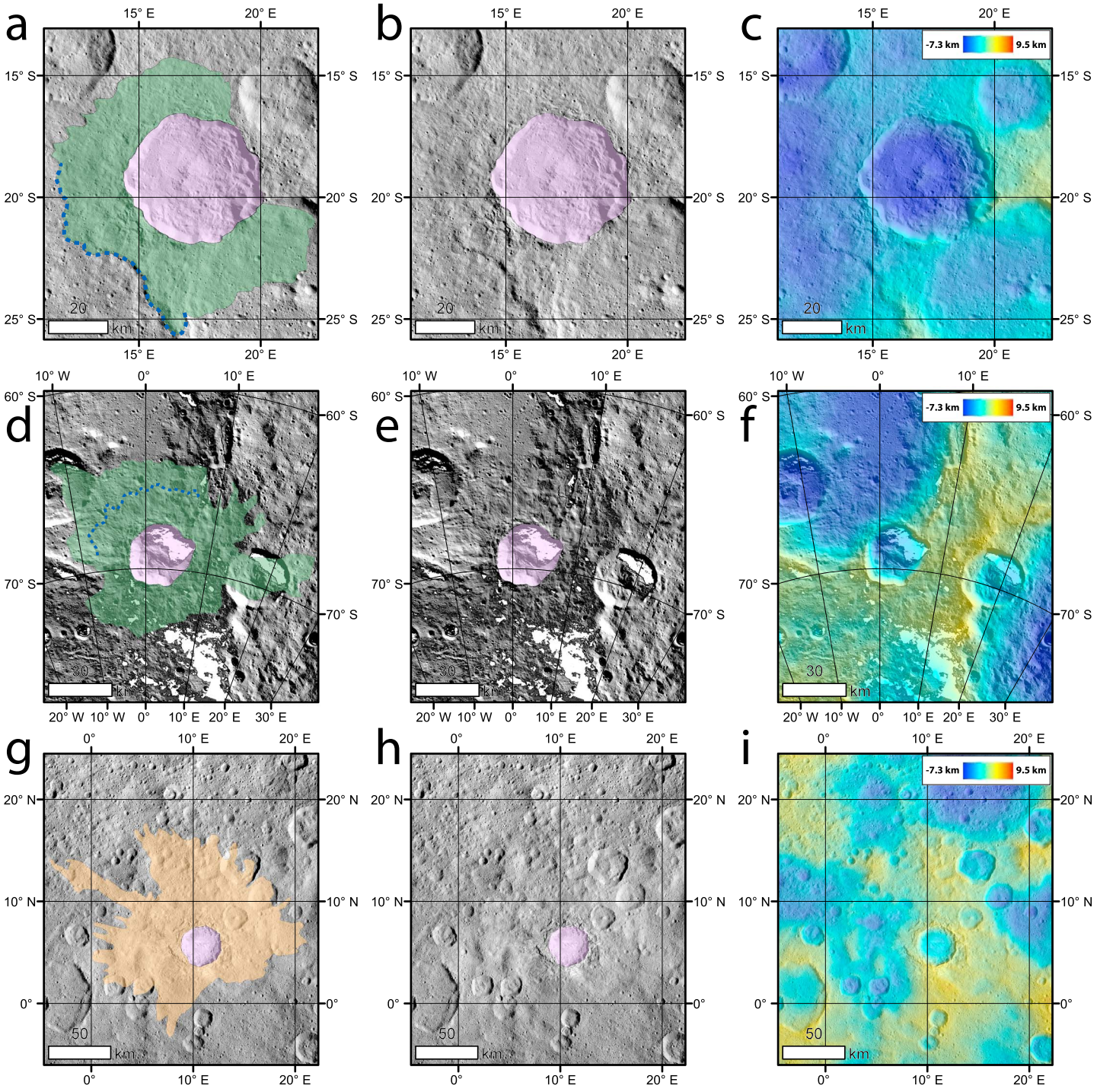

Figure 2. Three representative examples of cuspate/lobate and channelized FAE on Ceres. Mapped cuspate/lobate ejecta facies are represented by green overlays, channelized FAE are mapped with light orange overlays, and the source craters are mapped using light purple overlays. The dashed blue lines in (a) and (d) indicate regions of abruptly terminating ejecta similar to double layer ejecta on Mars and layered ejecta on icy satellites. (a) Kondo crater with mapped cuspate/lobate FAE deposit. (b) Same image from (a) but with ejecta related map overlays removed. (c) Same image as (a) but with all mapping overlays replaced by color-coded HAMO-derived topography. (d) Jacheongbi crater with mapped cuspate/lobate FAE deposit and possible double-layer behavior. (e) Same image from (d) but with ejecta related map overlays removed. (f) Same image as (d) but with all mapping overlays replaced by color-coded HAMO-derived topography. (g) Haulani crater with mapped channelized FAE deposit. (h) Same image from (g) but with ejecta related map overlays removed. (i) Same image as (g) but with all mapping overlays replaced by color-coded HAMO-derived topography. FAE = fluidized appearing ejecta; HAMO = High Altitude Mapping Orbit.

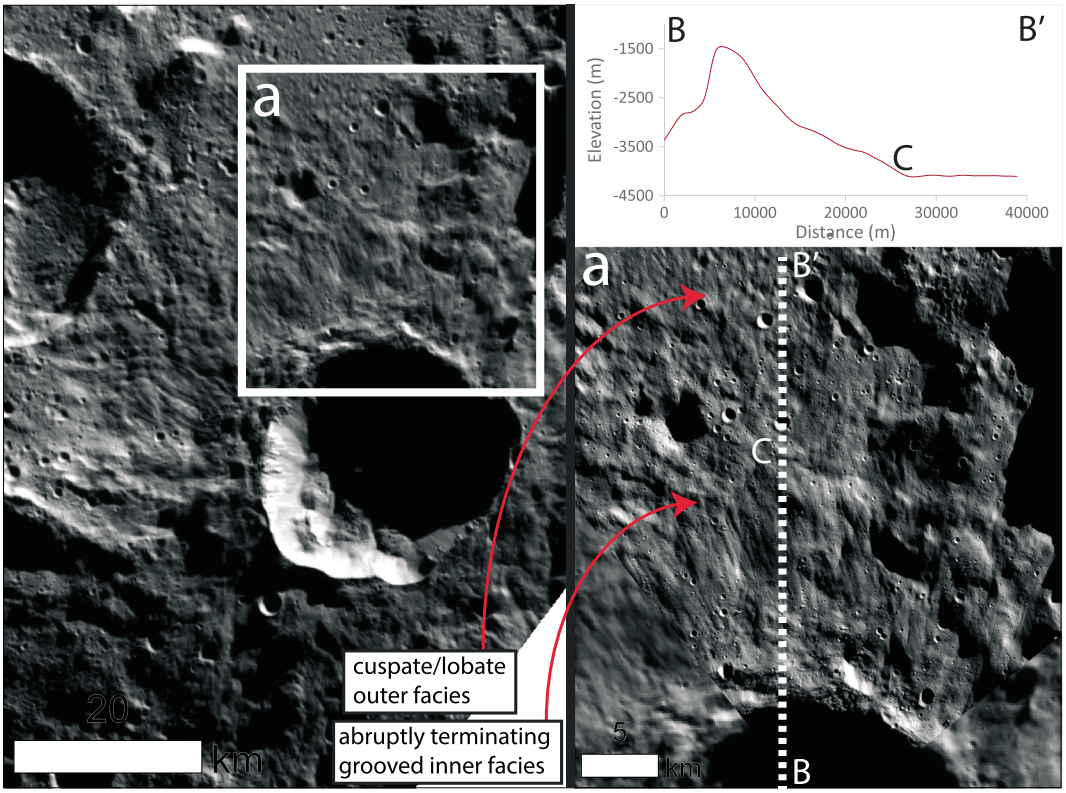

Figure 3. Expanded view of Jacheongbi crater and the northern portion of its cuspate/lobate FAE deposit as seen in Figures 2d–2f. In inset (a) note the arcuate-to-cuspate v-shaped lobes near the upper red arrow. This morphology is common among the outer facies of double- and multiple-layered ejecta on Mars as well as the other cuspate/lobate Cerean FAE and were used, in part, to help determine the outer margins of cuspate/lobate ejecta facies. The inner ejecta facies near the lower red arrow in inset (a) displays superimposed longitudinal grooves and an abruptly terminating margin, which is noticeable in the included topographic cross-section. These characteristic are often associated with the inner ejecta facies of Martian double layer ejecta. FAE = fluidized appearing ejecta.

In order to test for any latitudinal trends in the populations of Cerean FAE, we estimated their distribution functions using kernel density estimation (KDE) (Parzen, 1962; Rosenblatt, 1956). KDE is a nonparametric method for estimating the probability density function of a random variable. It is particularly useful in the case of Cerean FAE as we have no a priori knowledge of their distribution, and given the relatively small amount of data traditional statistical parameters such as the mean and variance are of limited utility. The only subjective choices made in the KDE analysis were kernel form and bandwidth. We chose to use Gaussian kernels and employed a modified Silverman's rule of thumb (equation (1)) to select a bandwidth that minimized the mean integrated squared error for each instance of the KDE analysis.

$$h = 0.9 \cdot \sigma \cdot N^{-0.2} \tag{1}$$

where in equation (1) h is the kernel bandwidth, σ is the standard deviation of the samples, and N is the number of samples (Silverman, 1986).

A complementary KDE analysis of the distribution of Cerean FAE with respect to their EM values was also carried out. The results of the global identification campaign and distribution analysis are summarized in section 3.1. This statistical analysis was completed using the Scikit-learn module for Python 3 (Pedregosa et al., 2011).

2.4. The Hybrid Kinematic-Dynamic Sliding Ejecta Emplacement Model

After measuring EM values and source crater radii, we tested the hypothesis that Cerean FAE could develop due to the presence of an H_2O-rich near-surface layer by using an analytic hybrid kinematic-dynamic sliding ejecta emplacement model. This model is similar to the one developed by Weiss and Head (2014) to

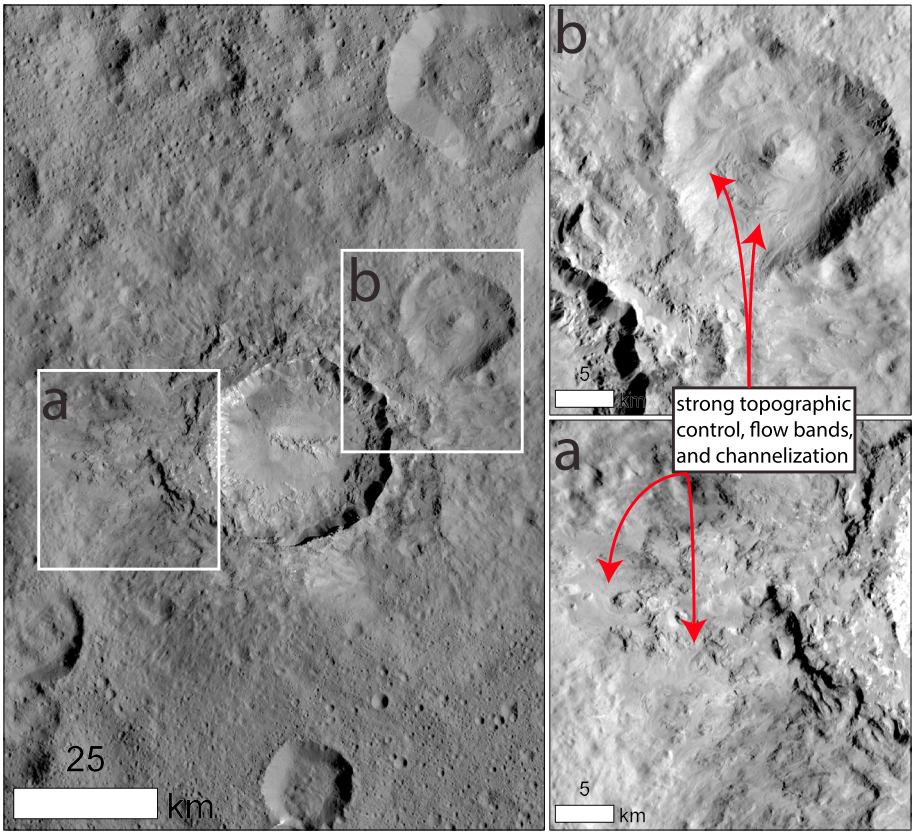

Figure 4. Expanded view of Haulani crater and the inner portions of its channelized FAE as seen in Figures 2g–2i. The thin-sheeted appearance, susceptibility to topographic control, and flow banding of the channelized FAE is highlighted in insets (a) and (b). This behavior is also observed at greater distances from the center of Haulani, albeit less dramatically. These morphological characteristics are common among channelized FAE on Ceres and were used to help delineate their boundaries. FAE = fluidized appearing ejecta.

approximate the EM for double-layer and low-aspect-ratio layered ejecta craters in ground ice-rich substrates on Mars, but with several key differences. Namely, we use full Newtonian gravity and do not assume a pure ice surface layer of variable thickness overlaying a rocky substrate, but rather, we assume an intimate mixture of silicates and water ice whose relative proportions are variable. Additionally, we assume a uniformly sloping substrate onto which the ejecta is deposited rather than a horizontal surface. A schematic representation of the kinematic-dynamic sliding ejecta emplacement model is displayed in Figure 5.

We also use Kraus et al.'s (2011) vaporization scaling law (equation (2)) to confirm that ejecta fluidization via melted and vaporized water is plausible on Ceres. In equation (2), M_V is the total mass of ice melted and vaporized, M_i is the mass of the impactor, T is the target material's temperature in kelvins, ψ is the impact angle measured from the horizontal, γ is the porosity, U is the average impact speed at Ceres, and $E_M(\gamma)$ is the specific internal energy for complete melting. Note that the results returned by equation (2) overestimate the mass of vapor produced by about a factor of two for impacts ~5 km/s (Kraus et al., 2011), which is the mean impact speed at Ceres (Marchi et al., 2016):

$$\log\left[\frac{M_{M+V}}{M_i}\right] = -0.53 + 0.0017\cdot T + 0.7\cdot\log[\sin\psi] + 0.46\cdot\gamma + \frac{3\cdot(0.554-0.07\cdot\phi)}{2}\cdot\log\left[\frac{U^2}{E_M(\gamma)}\right] \quad (2)$$

In this model we treat the FAE as ground-hugging continuous flows similar to landslides, debris flows, granular flows, or snow avalanches, which is consistent with how Martian fluidized ejecta have been interpreted to have been deposited and has been observed in laboratory ejecta experiments (e.g., Jones et al., 2016; Mouginis-Mark & Baloga, 2006; Runyon & Barnouin, 2018). In the model proposed here (equation (3)) we

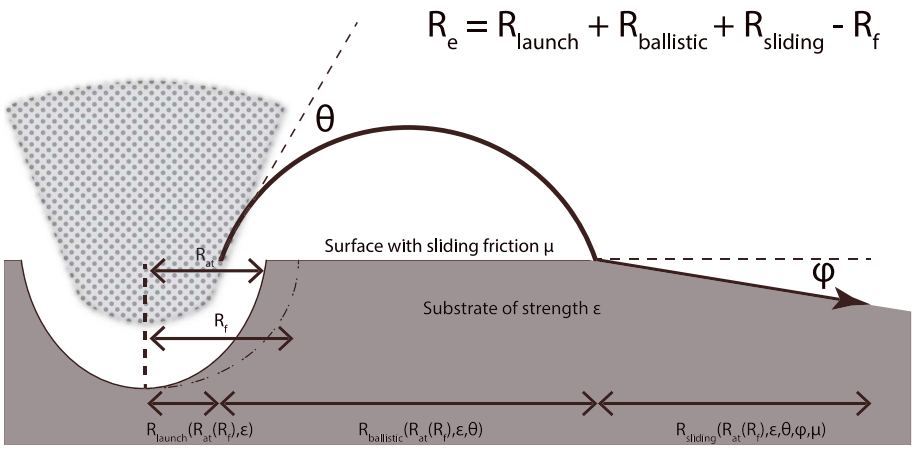

Figure 5. Schematic breakdown of the ejecta emplacement model (equation (3)) described in section 2.4. Note that the model is radially symmetric about the center of the source crater. The ejecta excavation angle, θ, is measured upward from the horizontal, while the mean surface slope, φ, is measured downward from the horizontal.

establish upper bound values for the coefficient of sliding friction encountered by FAE on Ceres by ignoring flow within the cohesive mass of ejecta. This approximation assumes that the Cerean FAE deposits were emplaced primarily as basal glides (i.e., flows that exhibit generally low velocity gradients throughout the entire depth of the flow, except at the sliding interface: Baloga et al., 2001). This assumption is justified by the morphological similarities between these Cerean flows and Martian layered ejecta, which along with Martian and Cerean long-runout landslides have been interpreted as basal-glide-emplaced features (Barnouin-Jha et al., 2005; Chilton et al., 2019; Schmidt et al., 2017). It should be noted, however, that Martian-style rampart ejecta are thought to require appreciable velocity gradients to form (Weiss & Head, 2018). We do not consider these cases separately as unambiguous ramparts have not been detected on Ceres. While it remains unknown if Martian layered ejecta or Cerean FAE behave predominantly like flows emplaced by basal gliding, the coefficient of sliding friction in our model remains a general proxy for dissipative forces. Thus, even if basal gliding does not play a significant role in the emplacement of these flows this model will still provide insight into the viscosity, degree of fluidization, and volatile content of these deposits (Wada & Barnouin-Jha, 2006; Weiss & Head, 2014). Since Ceres has no appreciable atmosphere our model does not take atmospheric effects into account.

From Newtonian gravity and Newton's second law it can be shown that the expected ejecta runout distance, R_e, is given by

$$R_e = R_{\text{flight}} + R_{\text{sliding}} + R_{\text{launch}} - R_f \tag{3}$$

The leftmost term on the right side of equation (3) is the ballistic flight contribution to the overall ejecta runout distance, R_{sliding} is surface sliding contribution, R_{launch} is the distance relative to the center of the crater where the volume-averaged ejecta is effectively sourced from, and R_f is the observed source crater radius. The components of R_{flight} and R_{sliding} are further described below

$$R_{\text{flight}} = 2 \cdot R_0 \cdot \left[\pi - \cos^{-1} \left(\frac{1}{\epsilon} \cdot \left\{ \frac{R_0 \cdot (U_{\text{VA}} \cdot \cos\theta)^2}{G \cdot M} - 1 \right\} \right) \right] \tag{4}$$

$$R_{\text{sliding}} = \frac{(U_{\text{VA}} \cdot \cos\theta \cdot \cos\varphi - U_{VA} \cdot \sin\theta \cdot \sin\varphi)^2}{2 \cdot g \cdot (\mu \cdot \cos\varphi - \sin\varphi)} \tag{5}$$

Here R_0 is the mean radius of Ceres, g is the mean surface gravitational acceleration on Ceres, μ is the coefficient of sliding friction of the surface, θ is the excavation angle, φ is the mean surface slope of the substrate, M is the mass of Ceres, G is the gravitational constant, ϵ is the eccentricity (equation (6)) of the volume averaged ejecta's suborbit, R_{at} is the apparent transient crater radius (equation (7)), and U_{VA} is the volume averaged ejecta velocity (equation (8)). R_{launch} is calculated by applying the mean value theorem to equation (8) after U_{VA} has been determined for a given R_{at}.

$$\epsilon = \left[1 + \frac{\left(U_{VA}^2 - \frac{2 \cdot G \cdot M}{R_0}\right)\left(R_0 \cdot U_{VA} \cdot \cos\theta\right)^2}{\left(G \cdot M\right)^2}\right]^{\frac{1}{2}} \tag{6}$$

$$R_{at} = \frac{\left(R^*\right)^{\eta} \cdot R_f^{1-\eta}}{1.3 \cdot \kappa} \tag{7}$$

$$U_{VA} = \int_{R_b(R_{at})}^{R_{at}} v_i(r) \cdot \frac{1}{3} \cdot \frac{\pi \cdot r^2}{V(R_{at}) - V(R_b)} dr \tag{8}$$

In equation (7) for the apparent transient crater radius (Holsapple, 1993; Melosh, 1989), R^* is the simple-to-complex transition radius on Ceres, which is approximately 5.15 km (Hiesinger et al., 2016). Both η and κ are numerically determined constants found to be approximately 0.04 ± 0.02 and 1.19 ± 0.04, respectively, in ice at the temperature of the icy Jovian satellites (Kraus et al., 2011; Senft & Stewart, 2011), which is broadly representative of the conditions at Ceres.

The relationship in equation (8) derives the volume averaged ejecta velocity over the expected excavated paraboloid, $V(R_{at})$ given by equation (9) (Melosh, 1989), minus the paraboloidal core of ejecta, $V(R_b)$, that exceeds the escape velocity of Ceres. U_{VA} is generated by averaging the launch velocities of paraboloidal shells of ejecta at given radial distances away from the center of impact, as given by the Richardson et al. (2005) scaling relationship (equation (10)), weighted by the volume of ejecta lofted at each specific velocity. The lower bound of integration in equation (8), R_b, is calculated by numerically solving equation (10) for R at $v_i = v_{escape}$ (for Ceres $v_{escape} \approx 510$ m/s).

$$V(R) = \frac{1}{9} \cdot \pi \cdot R^3 \tag{9}$$

$$v_i(R) = \frac{2 \cdot \sqrt{R_{at} \cdot g}}{1 + \varepsilon}\left[\left(\frac{R}{R_{at}}\right)^{-\varepsilon} - \left(\frac{R}{R_{at}}\right)^{\lambda}\right] \tag{10}$$

In the above equations R is the radial coordinate away from the center of impact, ε is the experimentally determined target strength, and λ is an arbitrary large constant chosen such that v_i goes to zero as R approaches R_{at}.

For our investigation establishing the plausibility of generating FAE through the incorporation of melt and vapor phases, we used nondimensionalized scaling from Melosh (1989) to determine the relationship between R_{at} and R_i, the impactor radius.

$$\pi_D = 1.24 \cdot \left(\frac{\rho_t}{\rho_p}\right)^{\frac{1}{3}} \cdot \frac{R_{at}}{R_i} \tag{11}$$

$$\pi_2 = \frac{3.22 \cdot g \cdot R_i}{U^2} \tag{12}$$

$$\pi_D = C_D \cdot \pi_2^{-\beta} \tag{13}$$

In equation (13) C_D and β are experimentally determined constants taken to be 2.5 ± 0.5 and 0.16 ± 0.02 in ice-like material at 150 K (Kraus et al., 2011). A complete list of model parameters and parameter ranges is given in Table 1.

Representative shock pressure, melt and vapor fraction, crater scaling, and volume averaged ejecta velocity relationships from equations (2), (7), (8), and (11)–(13) are shown in Figure 6.

We implemented the sliding ejecta emplacement model (equation (3)) for a range of plausible Ceres parameters outlined in Table 1 and compared the results to the slope corrected EM behavior of the channelized and cuspate/lobate FAE. In order to best characterize the most probable values of ε and μ over the entire parameter space of observed slope corrected EM and R_f values, we evaluated the emplacement model using a Monte Carlo-style analysis at $\varphi = 7.5°$ for R_e and EM values within the range $0 \text{ m} \leq R_e \leq 50{,}000$ m and $0.5 \leq \text{EM} \leq 6$ using randomly generated values for ε and μ confined to the ranges $1.8 \leq \varepsilon \leq 2.6$ and

Table 1
Sliding Ejecta Emplacement Model Parameters

Parameter	Symbol	Value
Crater collapse constant	κ	1.19 (ice at 150 K; Kraus et al., 2011) 1.0 (competent rock; Holsapple, 1993)
Crater collapse power	η	0.04 (ice at 150 K; Kraus et al., 2011) 0.079 (competent rock: Holsapple, 1993)
Crater scaling constant	C_d	2.5 (ice at 150 K; Kraus et al., 2011) 1.6 (competent rock; Melosh, 1989)
Crater scaling power	β	0.16 (ice at 150 K; Kraus et al., 2011) 0.22 (competent rock; Melosh, 1989)
Coefficient of sliding friction	μ	0.01–0.8
Ejecta scaling power	λ	6 (Richardson et al., 2005)
Excavation angle	θ	70° (Senft & Stewart, 2008)
Gravitational constant	G	$6.674 \cdot 10^{-10}$ $m^3/(kg{\cdot}s^2)$
Impactor density	ρ_p	920 kg/m^3 (ice) 2,800 kg/m^3 (CV chondrite; Consolmagno et al., 2008)
Impact speed	U	5.1 km/s (Ceres: Marchi et al., 2016)
Simple-complex transition radius	R^*	5.15 km (Ceres: Hiesinger et al., 2016)
Surface gravity	g	0.28 m/s^2 (Ceres)
Target density	ρ_t	1,290 kg/m^3 (Ceres: Ermakov et al., 2017)
Target porosity	γ	0.0–0.6
Target strength parameter	ε	1.8 (rock: Melosh, 1989; Weiss & Head, 2014) 2.6 (ice: Melosh, 1989; Weiss & Head, 2014)
Target temperature	T	150 K (Hayne & Aharonson, 2015)

Note. The parameters are listed alphabetically.

$0.01 \leq \mu \leq 0.8$. Coordinate pairs whose R_e value was a multiple of 1250 m and EM value was a multiple of 0.2 comprised the grid over which the model was implemented; the ε and μ values between grid points were estimated using cubic interpolation. In this analysis, the acceptable deviation from a prescribed EM value on the model grid for a randomly generated ε-μ pair was ±1%. The ε-μ pairs returned by the model represent the mean values of all the Monte Carlo generated ε-μ values that satisfied the aforementioned tolerance for a given R_f-EM coordinate pair. This was done in order quantify the variance of ε and μ for given EM values and to establish the sensitivity of the model to changes in ε and μ. For each R_f-EM coordinate pair within the model grid analyzed by the Monte Carlo-style analysis, 100,000 ε-μ pairs were considered. Increasing the number of iterations by an order of magnitude in general only changed the returned values of ε and μ by 0.3% and 0.01%, respectively. The results of this analysis are presented in section 3.2. Additionally, we applied this Monte Carlo technique to the specific R_f-EM coordinate pairs of all the identified Cerean FAE at their measured average local slope (Table 2).

While methane clathrate hydrates, which may compose a significant component of the upper layer of Ceres (Fu et al., 2017), display significantly higher material strength than pure water ice at low to modest strain rates (Choukroun et al., 2013), the overall magnitudes of their strengths likely becomes comparable at impact cratering strain rates (Jia et al., 2016). Unfortunately, the range of the coefficient of sliding friction for methane clathrate is poorly understood, as is the effect of clathrate dissociation during deformation on the runout efficiency of FAE (Durham et al., 2003). Thus, it remains unclear from the results of this model if and how methane clathrates contribute to the strength and frictional properties of the Cerean near surface.

3. Results

3.1. Geospatial and EM Distribution of FAE on Ceres

In total 30 individual Cerean ejecta blankets were found to exhibit morphologies suggestive of fluidization. These Cerean FAE craters were observed between absolute latitudes of 70°. While FAE forming craters are generally distributed uniformly in this latitude range, they display a slight affinity for the midlatitudes on the southern hemisphere (Figure 7). This is especially true of the 19 cuspate/lobate FAE, which show a moderately peaked distribution centered over the southern mid latitudes, while displaying decreased abundance in the northern hemisphere. The 11 channelized FAE display a much more uniform distribution at absolute

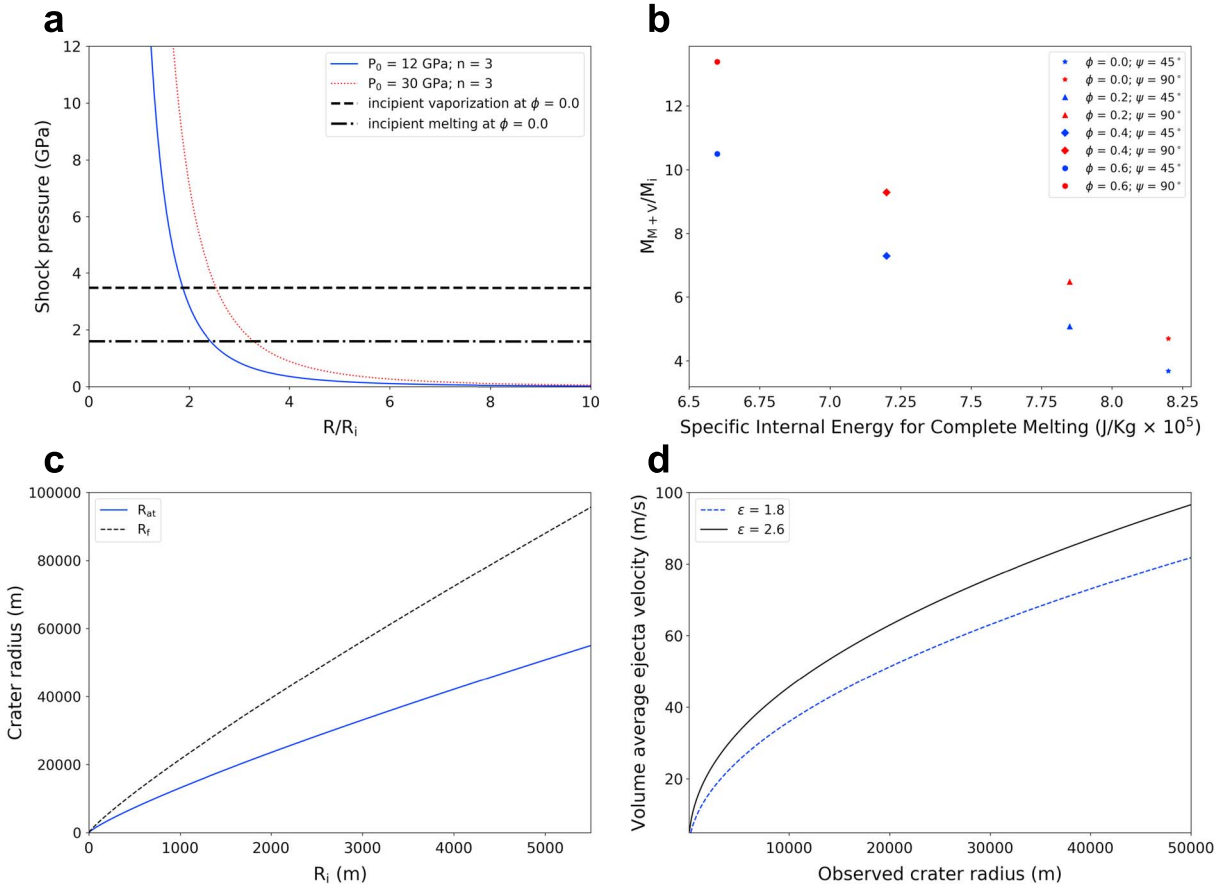

Figure 6. (a) Shock pressure as a function of the ratio of the radial distance away from the center of an impact over the impactor radius. The $P_0 = 12$ GPa curve is calculated for a pure ice impactor ($\rho_p = 920$ kg/m^3), whereas the 30 GPa curve is calculated for an average CV impactor ($\rho_p = 2800$ kg/m^3; Consolmagno et al., 2008). The incipient melting and vaporization pressures for water ice at approximate Ceres conditions ($\phi = 0.0$ and $T = 150$ K) are 1.60 and 3.48 GPa, respectively (Kraus et al., 2011). (b) Mass of water ice melted and vaporized relative to the impactor mass as a function of specific internal energy for complete melting using Kraus et al.'s (2011) scaling relationship. In this case we use the average impact speed at Ceres of 5.1 km/s such that the specific internal energy for complete melting is solely a function of porosity. The mass ratios plotted are reduced by a factor of 2 from equation (2) to reflect the departure from the scaling relationship observed at impact speeds less than 8 km/s (Kraus et al., 2011). (c) Final and apparent transient crater radii as a function of impactor radius; the scaling relationships are taken from Melosh (1989) and Holsapple (1993), while the relevant proportionality constants are taken from Kraus et al. (2011). (d) Magnitude of the volume averaged ejecta launch velocity as a function of final crater radius for the limiting cases of $\varepsilon = 1.8$ and $\varepsilon = 2.6$. The aforementioned values of ε are for competent silicate rock and water ice, respectively.

latitudes below ~50°, despite their slight preference for the northern hemisphere, but quickly become sparser at higher latitudes. The FAE on Ceres do not display any systematic trends with longitude nor do we observe any preferred flow orientation with geographic location.

In order to compare the Cerean FAE to each other as objectively as possible, the observed EM value of each instance of FAE was corrected to an effective EM value with a regional slope of $\varphi = 7.5°$, the average regional slope away from the source crater rim for all measured FAE craters. This was done using equation (3), the average regional slopes for each instance of FAE measured from the DTM using the mapped polygons (e.g., Figure 2), and the ε-μ pairs for each FAE deposit determined from section 3.2. The full range of observed EM values among Cerean FAE is 0.58–3.71, while the full slope corrected range is 0.58–4.9. Attributes of the Cerean FAE craters are displayed in Table 2.

The latitudinal locations of each class of Cerean FAE as a function of their mobility and the distribution of their observed and slope corrected EM values are shown in Figure 8. Figures 8a and 8b show the latitudinal locations and KDE-derived distributions for the observed EM values of the FAE. These plots show both a qualitative and quantitative difference in the observed EM behavior between the channelized and cuspate/lobate FAE populations on Ceres. From Figure 8b we note that both distributions are broadly

Table 2
Measured and Model Derived Properties of the 30 Identified Cerean FAE

Longitude	Latitude	Observed crater radius (m)	Observed EM (R_e/R_f)	Mean regional slope (degrees)	Model derived ε	Model derived μ	EM values corrected to 7.5° mean slope	FAE type	Crater name
−104.22	−66.37	22,410	0.59	4.83	2.19	0.25	0.94	cuspate/lobate	Sekhet
−131.06	−6.54	17,220	0.68	8.89	2.21	0.38	0.58	cuspate/lobate	Lociyo
21.07	−10.00	9,070	0.68	6.70	2.26	0.41	0.73	cuspate/lobate	Unnamed
124.49	18.31	16,730	0.73	7.12	2.23	0.31	0.77	cuspate/lobate	Kokopelli
−107.64	59.22	27,290	0.77	5.91	2.21	0.23	1.11	cuspate/lobate	Datan
−72.72	45.37	12,090	0.85	11.43	2.22	0.44	0.59	cuspate/lobate	Cozobi
17.29	−19.27	22,050	0.90	6.75	2.23	0.24	1.05	cuspate/lobate	Kondos
97.66	23.43	18,100	0.90	8.48	2.22	0.30	0.78	cuspate/lobate	Aristaeus
77.49	−67.29	9,470	0.92	5.05	2.23	0.25	1.36	cuspate/lobate	Ratumaibulu
168.44	−35.88	11,640	0.97	7.99	2.23	0.31	0.91	channelized	Juling
110.82	−39.29	11,360	1.04	7.42	2.22	0.28	1.05	cuspate/lobate	Unnamed
−158.41	−54.39	16,720	1.07	7.58	2.21	0.25	1.06	cuspate/lobate	Unnamed
−81.57	−34.76	4,860	1.12	6.06	2.24	0.28	1.35	cuspate/lobate	Unnamed
46.04	−47.94	32,340	1.15	5.40	2.22	0.17	2.78	cuspate/lobate	Sintana
−87.68	−54.06	12,000	1.35	6.95	2.22	0.22	1.53	cuspate/lobate	Nunghui
−160.93	−11.39	7,550	1.39	6.52	2.22	0.23	1.69	cuspate/lobate	Unnamed
88.38	−32.37	18,350	1.41	7.85	2.22	0.23	1.29	channelized	Tupo
−93.93	−34.28	8,610	1.58	8.38	2.24	0.25	1.34	cuspate/lobate	Unnamed
−0.24	42.01	6,060	1.59	7.71	2.22	0.25	1.53	channelized	Oxo
−49.40	0.67	4,170	1.63	9.23	2.23	0.30	1.29	channelized	Xevioso
−59.80	−42.35	10,040	1.70	4.97	2.25	0.16	4.93	cuspate/lobate	Besua
−141.64	−6.71	23,920	1.90	9.01	2.20	0.22	1.22	channelized	Azacca
2.31	−69.23	14,820	2.02	6.04	2.20	0.16	4.07	cuspate/lobate	Jacheongbi
28.08	69.01	14,060	2.31	7.06	2.18	0.18	2.77	channelized	Shennong
−107.88	63.09	9,710	2.39	8.00	2.21	0.20	2.06	channelized	Unnamed
45.62	33.75	27,070	2.52	7.98	2.25	0.18	2.04	channelized	Ikapati
−120.67	19.81	46,060	2.58	8.83	2.21	0.19	1.40	channelized	Occator
173.19	−39.39	15,750	2.63	8.95	2.23	0.21	1.63	channelized	Kupalo
−154.56	7.74	2,310	2.74	10.30	2.21	0.27	1.70	cuspate/lobate	Unnamed
10.82	5.73	16,100	3.71	9.31	2.22	0.20	1.81	channelized	Haulani

Note. The fluidized appearing ejecta (FAE) craters are listed in ascending order according to observed ejecta mobility (EM) value.

Gaussian, but with significantly different widths. In the uncorrected data the channelized FAE appear to have generally higher mobilities than their cuspate/lobate counterparts with distributions peaked at EM values of approximately 2.3 and 0.9, respectively. Figures 8c and 8d show a recapitulation of 8a and 8b, but with all the FAE's EM values corrected to a uniform substrate slope angle of 7.5°. While both the channelized and cuspate/lobate FAE's slope corrected distributions in Figure 8d retain their broadly Gaussian shape, their separation is significantly reduced. The corrected channelized FAE distribution's peak is reduced to EM ≈ 1.4, while the corrected cuspate/lobate FAE peak is increased to EM ≈ 1.1. Additionally, larger slope corrected EM values appear to correlate with higher latitudes (Figure 8c); however, this conclusion is based on only six data points. These FAE are also distinguishable as the six outlying EM data in Figure 8d.

3.2. Ejecta Emplacement Modeling

Figure 9 displays the slope corrected EM values for both populations of FAE superimposed on to the ε-μ parameter maps returned by the Monte Carlo-style analysis using the ejecta emplacement model. Specifically, the parameter spaces in this figure are constructed from the model generated ε and μ grids (see supporting information Data Sets S1 and S2). These grids were cubically interpolated to form continuous parameter spaces that were then discretized into the color ranges displayed in Figure 9 for ease of interpretation.

Inspecting Figure 9a, it is clear that the dependence of EM on ε is weak for FAE whose EM and source crater radii exceed 1 and 10,000 m, respectively. Additionally, the blotted texture of Figure 9a suggests that the variance in the expected value of ε for a given R_f-EM coordinate pair is significant. In comparison, Figure 9b reveals a strong dependence of EM on μ. This is especially true for EM values less than 3. There is also no

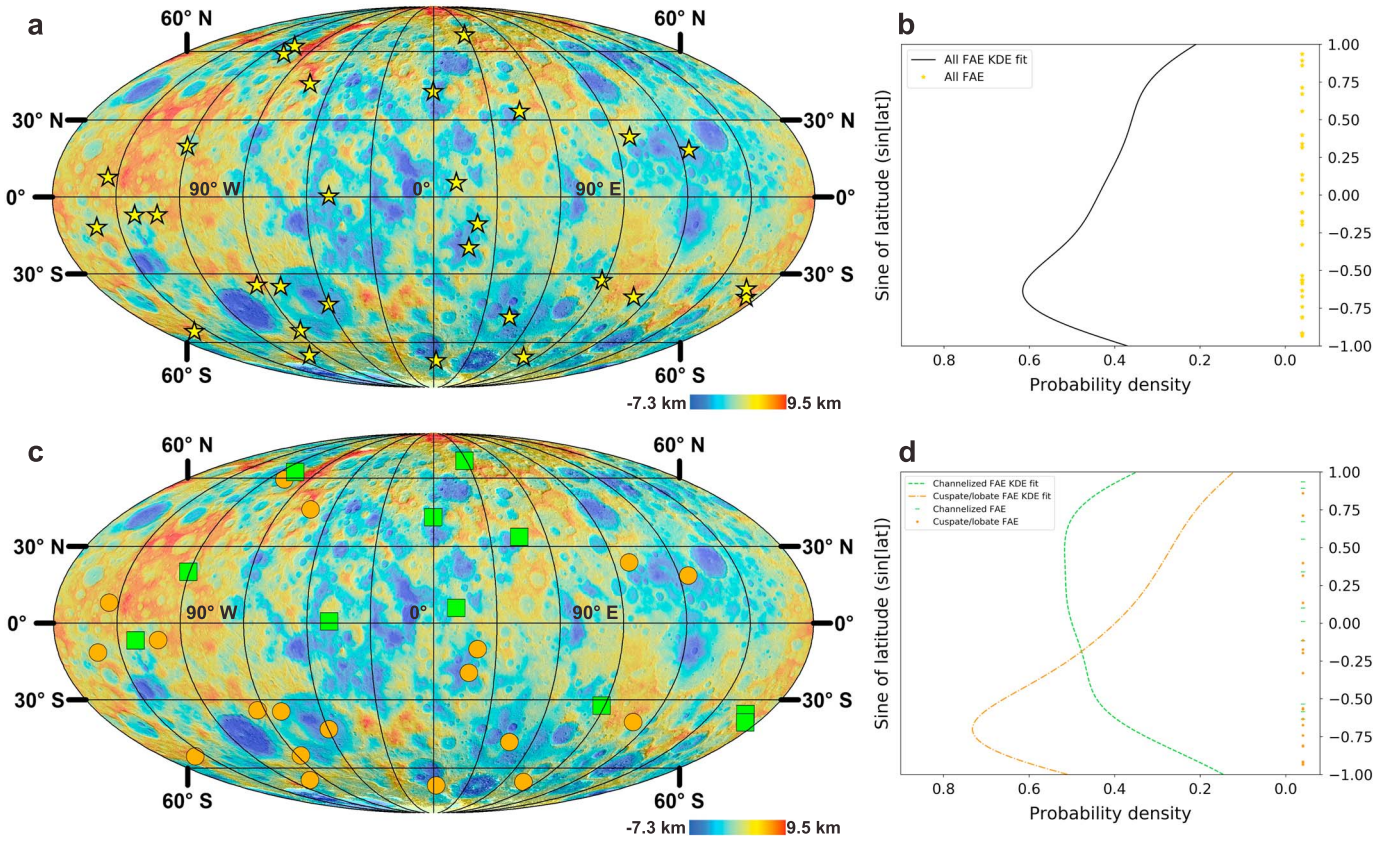

Figure 7. Global map and latitudinal distribution estimates for all FAE on Ceres. (a) Prime meridian centered Mollweide projection of Ceres, identified FAE are indicated by gold stars. (b) Normalized KDE latitudinal distribution function for all FAE on Ceres. Note the peak in the distribution around the southern mid latitudes. (c) Recapitulation of subfigure (a) displaying the Cerean FAE subdivided into their channelized (green squares) and cuspate/lobate (orange circles) populations. (d) Normalized KDE latitudinal distribution functions for the channelized and cuspate/lobate FAE populations. Note the preference for southern mid latitudes displayed by the cuspate/lobate FAE, and the more uniform distribution displayed by the channelized FAE. In panels (b) and (d) sine of latitude is used to correct for the decrease in area per latitudinal band toward the poles due to Ceres' spherical geometry. FAE = fluidized appearing ejecta; KDE = kernel density estimation.

indication that there is significant variance in the expected values of μ from this figure. The full range of both ε and μ for the channelized and cuspate/lobate FAE, as well the model mean variances of these parameters are summarized in Table 3. A two-dimensional KDE analysis of the model derived ε and μ values for each population of Cerean FAE is shown in Figure 10.

4. Discussion

4.1. Interpretation of the Geospatial and EM Distribution of FAE on Ceres

The 30 FAE on Ceres we identify in this study represent a substantial increase in described features from Schmidt et al.'s (2017) catalogue of Type 3 flows. This is not surprising given that the identification campaign presented in this study was conducted entirely at LAMO resolution. We also broadened the scope of our search to include morphological characteristics specific to fluidized ejecta/abruptly terminating ejecta. The two largest craters in the southern hemisphere of Ceres, Urvara and Yalode, as well as Dantu in the northern hemisphere were observed to have morphological elements consistent with our criteria for FAE. However, their characterization proved highly ambiguous due to the size of these craters and their ejecta blankets, their complex and varying morphologies, and their subsequent overprinting by younger impacts. Thus, they were excluded from our list of Cerean FAE craters.

Duarte et al. (2019) completed a survey of all lobate deposits on Ceres with characteristics intermediate to the Types 1–3 endmembers discussed by Schmidt et al. (2017). In their analysis they identify a number of Type 3 and intermediate lobate deposits that share morphological similarities with both fluidized ejecta and long

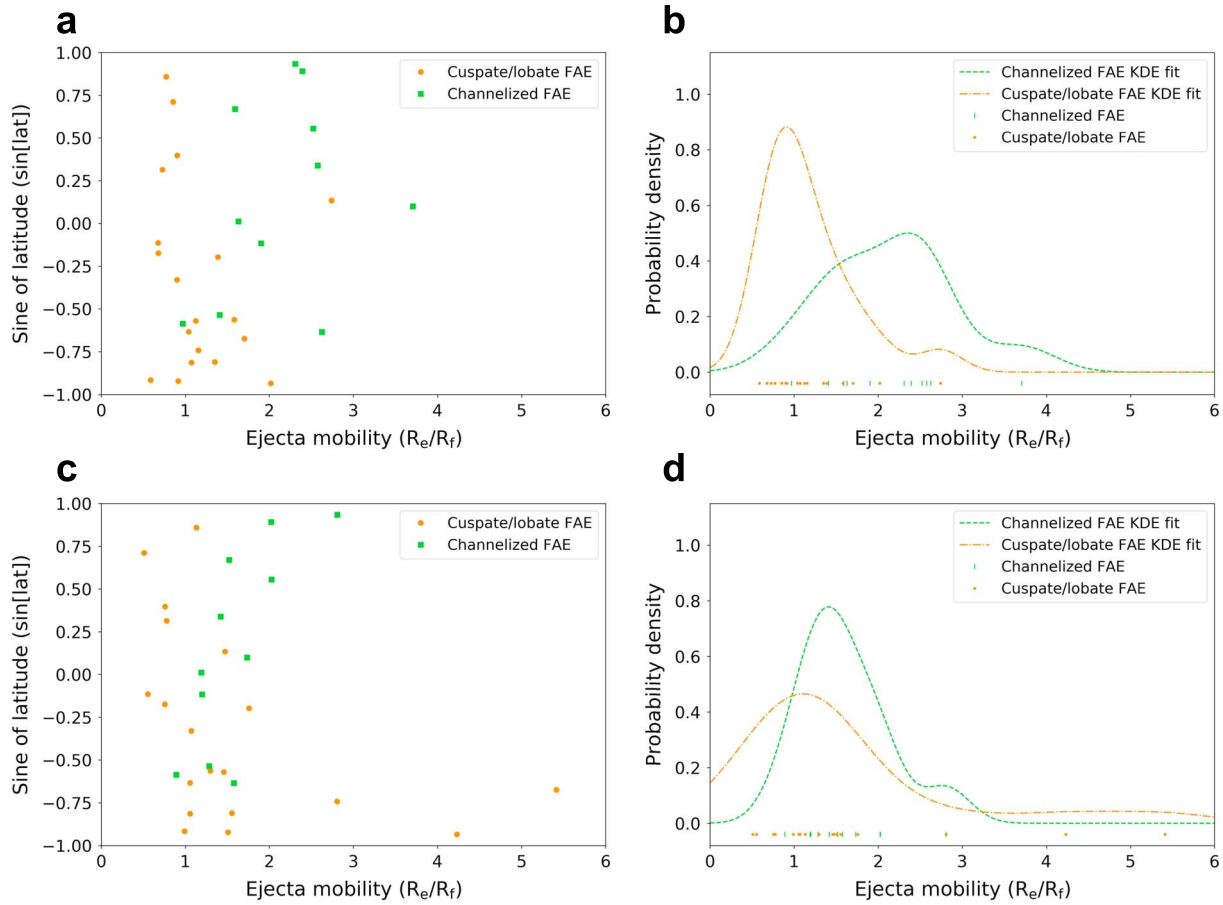

Figure 8. (a) Plot of the latitudinal distribution of the cuspate/lobate (orange circles) and channelized (green squares) Cerean FAE as a function of their observed (i.e., uncorrected) EM values. (b) Normalized KDE analysis of the observed EM distribution functions for the cuspate/lobate and channelized FAE. (c) Plot of the latitudinal distribution of the cuspate/lobate (orange circles) and channelized (green squares) Cerean FAE as a function of their 7.5° slope corrected EM values (i.e., the EM value for each FAE was adjusted using the model outlined in section 2.4 as if its mean regional radial slope was 7.5°). (d) Normalized KDE analysis of the slope corrected EM distribution functions for the cuspate/lobate and channelized FAE. Note the slight increase in mobility of FAE at higher latitudes in the slope corrected panel (c). The point markers in (b) and (d) indicate the locations of each individual FAE on the EM axis. In panels (a) and (c) sine of latitude is used to correct for the decrease in area per latitudinal band toward the poles due to Ceres' spherical geometry. FAE = fluidized appearing ejecta; KDE = kernel density estimation; EM = ejecta mobility.

runout landslides that are only identified as FAE in this manuscript. While we do not attempt to characterize landslide behavior in this study, we note that some of the FAE on Ceres have superimposed layers interior to their main ejecta apron with landslide-like morphologies. These features are similar in form to double-layer ejecta (e.g., Figure 3) but have much more muted morphologies than their Martian counterparts (Weiss & Head, 2013 and 2018). These deposits seldom have well-developed source scars near the outside of their source crater rims and have similar surface textures to their underlying ejecta layers. This suggests they were formed contemporaneously with the formation of the FAE source crater, or shortly thereafter as part of the modification stage. The diversity of proximal and colocated landslide-like deposits with FAE on Ceres is consistent with the interpretation that they are mobilized by ground ice (Chilton et al., 2019; Duarte et al., 2019; Schmidt et al., 2017).

From the latitudinal KDE analysis in Figure 7b we see that the distribution of all Cerean FAE is enhanced in the low to middle latitudes of the southern hemisphere. This is broadly consistent with the increased number density of Type 3 flows at low latitudes observed by Schmidt et al. (2017) but differs with respect to hemispherical preference of which they noted none. The subdivided channelized and cuspate/lobate FAE populations exhibit significantly different distributions with respect to latitude (Figures 7d); however, given the small number of FAE used in deriving these statistical class-specific distributions, we refrain from using them to draw any specific conclusions. While there is no consistent pattern to how Cerean FAE are

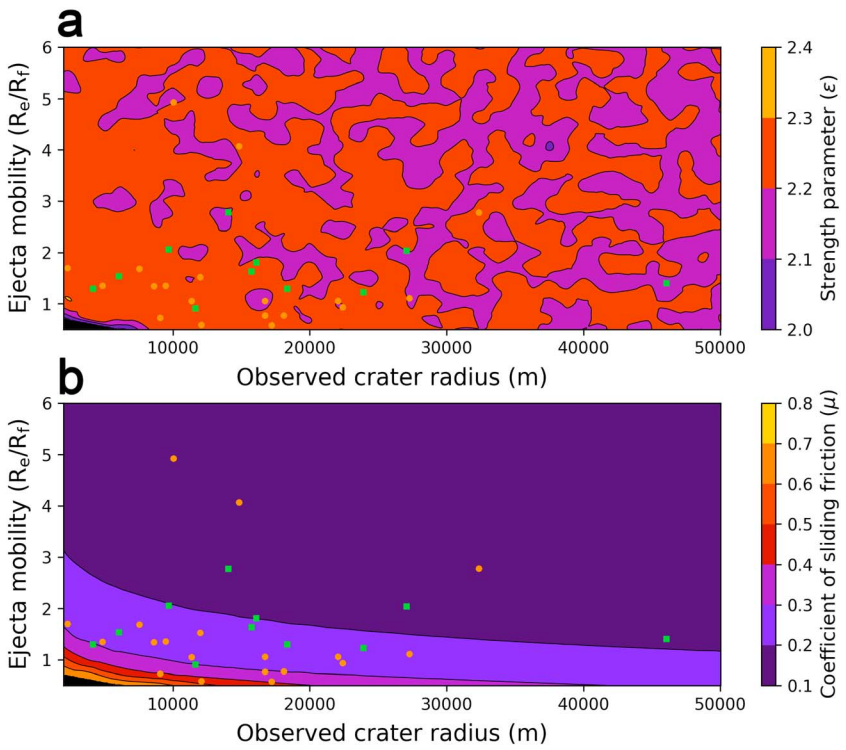

Figure 9. Results from the Monte Carlo-style analysis of the sliding ejecta emplacement model for cuspate/lobate (orange circles) and channelized (green squares) FAE. In both (a) and (b) observed final crater radius (R_f) is plotted on the horizontal axis, while slope corrected EM values are plotted against the vertical axis. The color contours in (a) indicate the model predicted values of the strength parameter, ε, as a function of R_f and slope corrected EM. The blotted texture in (a) suggests a weak dependence in the relationship between R_f and corrected EM on ε, and/or high variance in the model derived ε values for a given R_f-EM coordinate pair. (b) The model-predicted values of the coefficient of sliding friction, μ, as a function of R_f and slope-corrected EM. The close to horizontal behavior of the contours in (b) suggests that μ strongly influences the mobility of Cerean FAE. In (b), 80% of the identified FAE have μ less than 0.3. The black triangles in the bottom left of each plot represent parameter space that was not analyzed. FAE = fluidized appearing ejecta; EM = ejecta mobility.

distributed with respect to both latitude and longitude, we note that these features are slightly clustered around Yalode crater (292.48°E, 42.58°S) and the high standing Hanami Planum (230°E, 15°N), both of these areas contain an abundance of surface features which indicate the presence of significant quantities of near-surface ground ice (Sizemore et al., 2018). Additionally, Cerean FAE seem to be conspicuously absent from the low lying Vendemia Planitia (135°E, 23°N), Kerwan smooth material (124°E, 11°S), and much of the region composing the Ac-10 Rongo quadrangle (Platz et al., 2018). This supports the interpretation that near-surface ground ice on Ceres is distributed with a significant degree of heterogeneity (Bland et al., 2016; Sizemore et al., 2018).

The apparent association of Cerean FAE with geologically fresh appearing morphologies suggests that these features degraded rapidly on the surface after emplacement. This could plausibly be due to disruption and overprinting by subsequent impacts, micrometeorite bombardment and space weathering, sublimation of excavated volatiles, or any combination thereof. Our preferred interpretation for the channelized FAE is that they are deposited with a relatively high abundance of liquid water and water ice that both act as basal

Table 3
Model-Derived Parameter Ranges and Variances for ε and μ

FAE class	ε range	Mean model variance of ε (σ^2)	μ range	Mean model variance of μ (σ^2)
Channelized FAE	2.18–2.25	0.052	0.176–0.305	$1.3 \cdot 10^{-5}$
Cuspate/lobate FAE	2.19–2.26	0.052	0.159–0.438	$1.3 \cdot 10^{-5}$

Note. FAE = fluidized appearing ejecta.

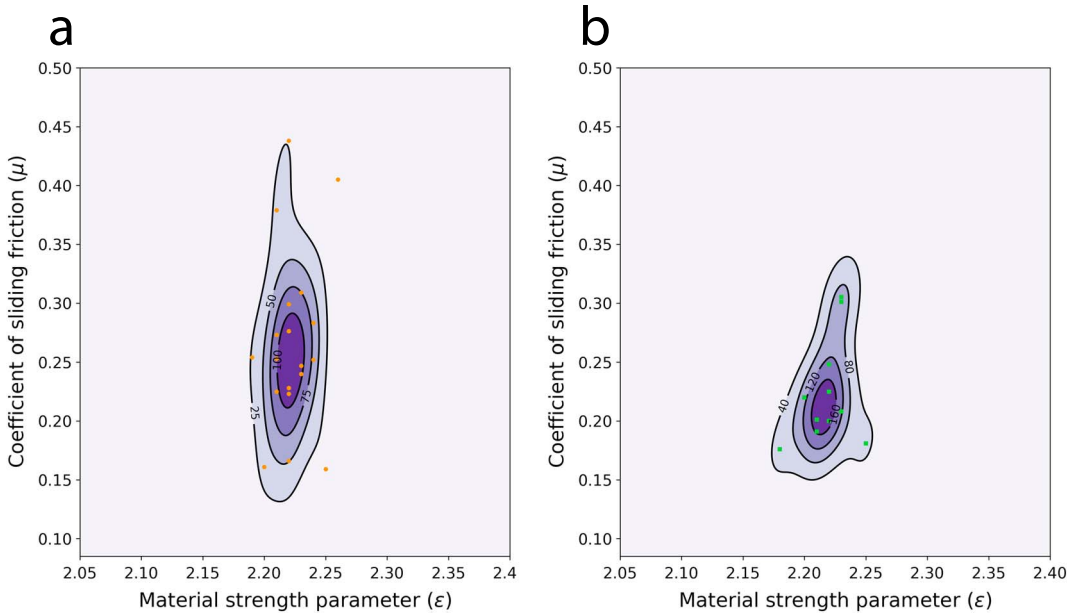

Figure 10. Two-dimensional kernel density estimation analysis of the model derived ε and μ values for the Cerean FAE. The labeled contour values are the probability density, with the color coding indicating increased probability with darkening color. Panel (a) shows the cuspate/lobate FAE (orange circle), while (b) displays the channelized FAE (green squares). FAE = fluidized appearing ejecta.

lubricants and reduce dissipative forces internal to the flow itself. Once refrozen, these pervasively ice rich deposits are highly susceptible to degradation by all of the aforementioned weathering processes. This interpretation is supported by the highly fluid nature, relative paucity, and extremely fresh morphologies of the channelized FAE. With one exception, all of the observed channelized FAE are located in areas where the regional downhill slope exceeds the average Cerean circumcrater slope of 7.5°. This behavior is not seen among cuspate/lobate FAE, who are observed to generally favor emplacement on downhill slopes shallower than this average. While this preference for different emplacement angles is largely subtle, it implies that reducing the effective coefficient of sliding friction and/or increasing the amount of expendable gravitational potential energy may favor the production of channelized FAE.

The cuspate/lobate FAE, which are generally more morphologically similar to abruptly terminating ejecta and Martian layered ejecta, are interpreted to be deposited predominantly as basal glides whose mobility is primarily governed by the lubricating effects of near-surface ground ice in the region immediately proximal to the FAE forming impact. A consequence of this interpretation is that the flow material itself need not necessarily have a high water content if the there exists an ample supply in the near surface. If cuspate/lobate FAE flows are depleted in water compared to channelized FAE, they would be relatively more resistant to volatile-loss-driven degradation processes such as deflation and impact induced sublimation. In general, cuspate/lobate FAE are observed in a multitude of degradation states across numerous source craters of varying relative ages, which supports the interpretation that they have a longer geologic lifetime than channelized FAE. The cuspate/lobate FAE are also observed to generally have qualitatively thicker deposits whose morphology is less frequently modified by preexisting topography relative to channelized FAE. This implies that cuspate/lobate FAE have high effective viscosities relative to their channelized FAE counterparts. This may be caused by increased interparticle friction due to reduced ice content of the material in motion relative to channelized FAE. Additionally, the thicker nature of cuspate/lobate FAE deposits likely helps preferentially preserve them relative to channelized FAE, at least at the resolution we used to identify them.

It is important to note that the morphologically based interpretation that channelized FAE have a higher bulk water content relative to cuspate/lobate FAE at the time of their deposition does not necessarily indicate a higher substrate ground ice volume fraction proximal to their source craters. This predicted increase in the water content of channelized FAE may be due to greater incorporation of warm ice or liquid water from

infrequent but exceptionally energetic impacts, rather than an increase in the ground ice content of the target materials. Since we interpret the mobility of cuspate/lobate FAE to be dominated by basal friction, a ground ice-rich substrate would still greatly reduce the friction experienced by these relatively drier flows.

4.2. Interpretation of the Sliding Ejecta Emplacement Model

The results presented in Figure 9 show that there is no robust distinction between the channelized and cuspate/lobate FAE populations in R_e-slope corrected EM space. Additionally, there are no robust clusters or families of FAE seen within this space.

It is clear from inspection of Figure 9a that for the R_e-slope corrected EM parameter space relevant to Cerean FAE their mobility is only weakly dependent on ε. The entire ε mean range of all forms of Cerean FAE is estimated from the model to be $2.18 \leq \varepsilon \leq 2.26$, while the mean model standard deviation (σ) for a given ε is 0.23 (Table 3). The mean value of ε for each population is 2.22, which is almost exactly intermediate behavior between competent rock ($\varepsilon = 1.8$) and water ice ($\varepsilon = 2.6$). The weak dependence of the model on ε manifests in the intermediate values and blotted texture of the entire ε parameter space. The intermediate values of the ε parameter space combined with its high variance suggest that a large range of material strengths could lead to similar EM values for a given crater radius and well-constrained μ value. Thus, the blotted texture in Figure 9a results from statistical noise in the Monte Carlo analysis due to the small amount of control ε exerts on the model derived EM values relative to μ, which is the dominant factor in determining its behavior. From the measurement and deviation of ε alone it is difficult to estimate the ground ice content of the substrate, but we do conclude that the substrate near these FAE, under impact cratering strain rates, mechanically behaves more like a ground ice rich ice-silicate mixture, and/or an extremely unconsolidated material, than competent rock. This is consistent with the low flexural rigidity reported by Hughson et al. (2019), for the Cerean crust near Nar Sulcus, and the low simple-to-complex transition diameter for impact craters observed by Hiesinger et al. (2016), which have been interpreted to make Ceres more mechanically akin to outer solar system icy satellites than terrestrial planets.

Unlike ε, inspection of Figure 9b shows a strong correlation between μ and slope corrected EM value. While the lower bounds on the range of μ values are similar for both the channelized and cuspate/lobate FAE, the upper bound μ value for the cuspate/lobate ejecta is significantly higher than its channelized FAE counterpart (see Table 3). The mean μ values for the channelized and cuspate/lobate FAE are 0.223 and 0.267, respectively, while the mean model standard deviation for a given μ is 0.0037. This implies higher amounts of sliding friction are acceptable for the formation of cuspate/lobate FAE compared to the channelized variety.

On Earth, supraglacial landslides typically have effective μ values between 0.015 and 0.2 (Weiss & Head, 2018). While this range is somewhat comparable to Cerean FAE, the upper bounds of their effective μ ranges are still larger by approximately a factor of 2. This is in part possibly due to the increase in sliding friction coefficient expressed by polycrystalline ice with decreasing temperature. At 263 K, the coefficient for ice-on-ice sliding friction is typically 0.01–0.15 (this value is strongly a function of sliding velocity), whereas at a Ceres appropriate 150 K this value is approximately 0.45 (De Blasio, 2014; Schulson & Fortt, 2012). In contrast, the typical values for the coefficients of sliding friction for common terrestrial silicate materials lie between 0.5 and 0.8 (e.g., Ramana & Gogte, 1989). From the ice-like range of μ values expressed by the Cerean FAE in combination with the expectation of a pore-saturating ice layer within a few meters of the surface, even at the equator, inferred from nuclear spectroscopy (Prettyman et al., 2017), we interpret that the low model-derived μ values for the observed FAE are most likely due to a combination of sliding on a ground ice-rich substrate and by fluidization due to the incorporation of impact melt fluids and/or basal lubrication due to melted near surface water ice. This is especially likely for the 80% of FAE whose μ values are under 0.3. This is also consistent with the melt/vapor productions volumes estimated from equation (2) shown in Figure 6b, and the morphological interpretations made in section 4.1. Due to a lack of experimental understanding, in formulating the previous interpretation, we assume that any clathrates present near the surface have similar frictional properties to pure water ice.

Alternatively, some craters on dry airless bodies, such as the Moon's King crater, have ejecta morphologies suggestive of some degree fluidization (Heather & Dunkin, 2003; Howard, 1972), and it has been postulated that lateral sliding of dry ejecta materials from purely ballistic sedimentation could lead to lobate

morphologies (Oberbeck, 1975). Strong vibrational motions from the initial impact shock may also help mobilize ejected material via acoustic fluidization (Melosh, 1979). Recent laboratory experiments by Runyon and Barnouin (2018) have further shown that dry ejecta deposited via ballistic sedimentation extensively shears the subsurface, embeds itself within the regolith, and exhumes regolith material via saltation all while sliding along the surface. Runyon and Barnouin (2018) go on to demonstrate that these interactions slightly increase the runout efficiency (which is the reciprocal of the drop height to runout length ratio: H/L) of dry ejecta relative to terrestrial rock avalanches. However, their measured runout efficiency values are broadly Earth-like in the context of mass wasting throughout the solar system. Since the reported runout efficiencies of putative Cerean FAE are generally higher than those of comparable terrestrial or Martian debris flows (Schmidt et al., 2017), we continue to prefer the interpretation that the enhanced mobility of FAE on Ceres is due to ground ice mediated friction reduction.

Using a simple areal mean approximation for the coefficient of sliding friction, similar to the method employed by De Blasio (2014) when analyzing terrestrial rock avalanches traveling on glaciers, we estimate an upper bound of ~30–50 vol.% water ice at a depth scale of at least 1–5 km proximal to each FAE source crater (depending on the size of the source crater). This range is derived from linearly mixing the μ value of ice, which is taken to be of order 0.01 at ejecta emplacement velocities, with μ values for common silicate materials, which are taken to be between ~0.5 and 0.8. The mixing model is constrained by the mean μ values derived for both classes of Cerean FAE, and the resulting fractional contribution of water ice to the overall coefficient of sliding friction is taken to be representative of its volumetric abundance in the near surface. This estimate is broadly consistent with the composition suggested by Fu et al. (2017); however, accurately including the effects of melt water lubrication would certainly reduce this estimate. It remains ambiguous as to whether this estimated near-surface ground ice content is ubiquitously true across Ceres, or if it only applies selectively to heterogeneous regions of enhanced ground ice content, but the slight affinities and aversions for certain geographical regions combined with the variable range of model estimated μ values displayed by Cerean FAE suggest that the latter is more representative of reality. This possibility was first postulated by Bland et al. (2016) to explain the radically different relaxation states of similar craters on Ceres. We interpret the physical properties and geographic distribution of FAE to be indicative of a modest global reservoir of pore filling ground ice in the upper few meters to kilometers on Ceres, which is subject to significant regional enrichment and depletion.

An underlying assumption of our model is that the volume-averaged ejecta is effectively excavated at an angle of 70° from the preimpact surface (Senft & Stewart, 2008). We consider this assumption to be appropriate for the bulk properties of ejecta sourced within 80% of R_{at}, which the volume averaged ejecta well approximates, for impacts into a substrate rich in buried water ice (Senft & Stewart, 2008). This is likely the case on Ceres. Nevertheless, accurately accounting for the effects of changing excavation angle, particularly how it decreases with increasing R_{at}, by incorporating numerical impact simulations for potential Ceres-like substrates would further increase the fidelity of this model.

5. Conclusions

We identified 30 instances of FAE on Ceres that display morphological elements (such as a sheeted or layered appearance, arcuate or cuspate terminal lobes, superimposed longitudinal grooves, and channelized deposits) commonly associated with fluidization. Two distinct morphological populations of FAE were identified: a channelized FAE population and a cuspate/lobate population. While both of these FAE types are distinctly Cerean, the channelized FAE display morphological characteristics common among fluid-rich debris flows, and the cuspate/lobate FAE share many morphological similarities with layered ejecta craters on Mars, Ganymede, Dione, and Charon. After mapping and quantifying the identified FAE, we searched for trends in their geographical and EM distributions. We also explored the hypothesis that the morphologies and various EM values of Cerean FAE can be explained by a combination of impacting into a low-cohesion target material, and sliding on a low-friction partially icy substrate. Our results show the following:

1. Two morphological classes of FAE exist on Ceres: channelized, and cuspate/lobate. Both the channelized and cuspate/lobate Cerean FAE have similarly distributed slope corrected EM values, with distributions peaked at EM = 1.4 and EM = 1.1, respectively. Despite their distinctive physical appearances, both channelized and cuspate/lobate FAE have similar model-derived ε and μ values.

2. FAE on Ceres are abundant at absolute latitudes less than 70°, above which their density rapidly decreases. The cuspate/lobate FAE display a slight affinity for the mid latitudes on the southern hemisphere. The channelized FAE display a more uniform distribution with respect to latitude.
3. The low model derived μ values for the majority of Cerean FAE are likely due to a combination of sliding on an intimate mixture of rock and ice, and by friction reduction caused by both fluidization through the incorporation of impact melt fluids and basal lubrication via melted near surface volatiles.
4. The vast majority of FAE source craters are modeled to have material strengths that are more ice like than rock like under impact cratering strain rates. This is consistent with previous observations of the low simple-to-complex transition diameter, and the reported low flexural rigidity of Ceres. This aligns Ceres more closely with icy satellites than terrestrial planets with respect to the mechanical properties of its outermost layer.
5. The widespread distribution of FAE in combination with results from nuclear spectroscopy suggest that pore filling ground ice is present only a few meters below the surface to at least 1–5 km based on crater ejecta excavation depths.

Our sliding ejecta emplacement model, despite its usefulness as a simple preliminary investigation tool, would be improved by higher fidelity constraints on the material strength and frictional properties of the shallow subsurface/surface. Laboratory experiments that better constrain these properties in Ceres regolith analogues would allow our model to better predict the composition of the near-surface of Ceres.

The identification and modeling of FAE on Ceres further cement its position as a volatile rich and geologically interesting world. The association of Cerean FAE with weak, volatile rich material makes them of particular interest for future in situ exploration of Ceres and further suggests that the geologic history of the Cerean near surface was significantly influenced by both physical and chemical water-rock interactions.

Acknowledgments
We thank NASA, DLR, MPS, and INAF for funding and enabling the Dawn mission as well as all the members of the Dawn flight, instrument, and science teams for their efforts that led to a successful mission at Ceres and the collection and processing of the data used in this study. This article benefited from constructive comments by the Associate Editor, D. K. Weiss, and one anonymous reviewer. All data utilized are available in NASA's PDS, under the Small Bodies Node (https://pds-smallbodies.astro.umd.edu/data_sb/missions/dawn/index.shtml). The model ε-μ output as a function of observed crater radius and EM is available in the supporting information for this article. This research was funded by the Dawn Mission Science Team, which is supported by NASA's Discovery program.

References

Baloga, S. M., Fagents, S. A., & Mouginis-Mark, P. J. (2005). Emplacement of Martian rampart crater deposits. *Journal of Geophysical Research*, *110*, E10001. https://doi.org/10.1029/2004JE002338

Baloga, S. M., Glaze, L. S., Peitersen, M. N., & Crisp, J. A. (2001). Influence of volatile loss on thickness and density profiles of active basaltic flow lobes. *Journal of Geophysical Research*, *106*(B7), 13,395–13,405. https://doi.org/10.1029/2000JB900475

Barlow, N. G. (2005). A review of Martian impact crater ejecta structures and their implications for target properties. Large Meteorite Impacts III, Kenkmann, T., Hörz, F., Deutsch, A. 433–442.

Barlow, N. G., Boyce, J. M. (2013). Martian low-aspect-ratio layered ejecta (LARLE) craters: Constraints on formation models from analysis of LARLE distribution and characteristics. Paper presented at Lunar Planet. Sci. XLIV. Abstract 1196.

Barlow, N. G., & Bradley, T. L. (1990). Martian impact craters: Correlations of ejecta and interior morphologies with diameter, latitude, and terrain. *Icarus*, *87*(1), 156–179. https://doi.org/10.1016/0019-1035(90)90026-6

Barlow, N. G., & Perez, C. B. (2003). Martian impact crater ejecta morphologies as indicators of the distribution of subsurface volatiles. *Journal of Geophysical Research*, *108*(E8), 5085. https://doi.org/10.1029/2002JE002036

Barlow, N. G., Pollak, A. (2002). Comparisons of ejecta mobility ratios in the northern and southern hemispheres of Mars. Paper presented at Lunar Planet. Sci. XXXIII. Abstract 1322.

Barnouin, O. S., Zuber, M. T., Smith, D. E., Neumann, G. A., Herrick, R. R., Chappelow, J. E., et al. (2012). The morphology of craters on Mercury: Results from MESSENGER flybys. *Icarus*, *219*(1), 414–427. https://doi.org/10.1016/j.icarus.2012.02.029

Barnouin-Jha, O. S., Baloga, S., & Glaze, L. (2005). Comparing landslides to fluidized crater ejecta on Mars. *Journal of Geophysical Research*, *110*(E4), E04010. https://doi.org/10.1029/2003JE002214

Barnouin-Jha, O. S., & Buczkowski, D. L. (2007). Comparing the runout distances of fluidized ejecta on Mars with mass movements on Earth. Paper presented at Lunar Planet. Sci. XXXVIII. Abstract 1304.

Barnouin-Jha, O. S., & Schultz, P. H. (1998). Lobateness of impact ejecta deposits from atmospheric interactions. *Journal of Geophysical Research*, *103*(E11), 25,739–25,756. https://doi.org/10.1029/98JE02025

Barnouin-Jha, O. S., Schultz, P. H., & Lever, J. H. (1999a). Investigating the interactions between an atmosphere and an ejecta curtain: 1. Wind tunnel tests. *Journal of Geophysical Research*, *104*(E11), 27,105–27,115. https://doi.org/10.1029/1999JE001026

Barnouin-Jha, O. S., Schultz, P. H., & Lever, J. H. (1999b). Investigating the interactions between an atmosphere and an ejecta curtain: 2. Numerical experiments. *Journal of Geophysical Research*, *104*(E11), 27,117–27,131. https://doi.org/10.1029/1999JE001027

Bland, M. T., Raymond, C. A., Schenk, P. M., Fu, R. R., Kneissl, T., Pasckert, J. H., et al. (2016). Composition and structure of the shallow subsurface of Ceres revealed by crater morphology. *Nature Geoscience*, *9*(7), 538–542. https://doi.org/10.1038/ngeo2743

Boyce, J., Barlow, N., Mouginis-Mark, P., & Stewart, S. (2010). Rampart craters on Ganymede: Their implications for fluidized ejecta emplacement. *Meteoritics & Planetary Science*, *45*(4), 638–661. https://doi.org/10.1111/j.1945-5100.2010.01044.x

Boyce, J. M., Barlow, N. G., Wilson, L. (2012). Model for the emplacement of the outer ejecta layer of low-aspect-ratio layer ejecta craters by turbulent flow. Paper presented at Lunar Planet. Sci. XLIV. Abstract 1196.

Boyce, J. M., & Mouginis-Mark, P. J. (2006). Martian craters viewed by the thermal emission imaging system instrument: Double-layered ejecta craters. *Journal of Geophysical Research*, *111*, E10005. https://doi.org/10.1029/2005JE002638

Buczkowski, D. L., Schmidt, B. E., Williams, D. A., Mest, S. C., Scully, J. E. C., Ermakov, A., et al. (2016). The geomorphology of Ceres. *Science*, *353*(6303), aaf4332. https://doi.org/10.1126/science.aaf4332

Carr, M. H., Crumpler, L. S., Cutts, J. A., Greeley, R., Guest, J. E., & Masursky, H. (1977). Martian impact craters and emplacement of ejecta by surface flow. *Journal of Geophysical Research*, *82*(28), 4055–4065. https://doi.org/10.1029/JS082i028p04055

Castillo-Rogez, J. C., & McCord, T. B. (2010). Ceres' evolution and present state constrained by shape data. *Icarus*, *205*(2), 443–459. https://doi.org/10.1016/j.icarus.2009.04.008

Chilton, H. T., Schmidt, B. E., Duarte, K., Ferrier, K. L., Hughson, K. H. G., Scully, J. E. C., et al. (2019). Landslides on Ceres: Inferences into ice content and layering in the upper crust. *Journal of Geophysical Research: Planets*, *124*. https://doi.org/10.1029/2018JE005634

Choukroun, M., Kieffer, S. W., Lu, X., & Tobie, G. (2013). Clathrate hydrates: Implications for exchange processes in the outer solar system. In M. Gudipati, & J. Castillo-Rogez (Eds.), *The science of solar system ices. Astrophysics and space science library* (Vol. 356, pp. 409–454). New York, NY: Springer. https://doi.org/10.1007/978-1-4614-3076-6_12

Combe, J. -P., McCord, T. B., Tosi, F., Ammannito, E., Carrozzo, F. G., De Sanctis, M. C., et al. (2016). Detection of local H_2O exposed at the surface of Ceres. *Science*, *353*(6303), aaf3010. https://doi.org/10.1126/science.aaf3010

Combe, J. -P., Raponi, A., Tosi, F., De Sanctis, M. C., Carrozzo, F. G., Zambon, F., et al. (2019). Exposed H_2O-rich areas detected on Ceres with the dawn visible and infrared mapping spectrometer. *Icarus*, *318*, 22–41. https://doi.org/10.1016/j.icarus.2017.12.008

Consolmagno, G. J., Britt, D. T., & Macke, R. J. (2008). The significance of meteorite density and porosity. *Chemie der Erde*, *68*(1), 1–29. https://doi.org/10.1016/j.chemer.2008.01.003

Costard, F. M. (1989). The spatial distribution of volatiles in the Martian hydrolithosphere. *Earth, Moon, and Planets*, *45*(3), 265–290. https://doi.org/10.1007/BF00057747

De Blasio, F. V. (2014). Friction and dynamics of rock avalanches travelling on glaciers. *Geomorphology*, *213*, 88–98. https://doi.org/10.1016/j.geomorph.2014.01.001

Duarte, K. D., Schmidt, B. E., Chilton, H. T., Hughson, K. H. G., Sizemore, H., Scully, J. E. C., et al. (2019). Landslides on Ceres: Diversity and geologic context. https://doi.org/10.1029/2018JE005673

Durham, W. B., Kirby, S. H., Stern, L. A., & Zhang, W. (2003). The strength and rheology of methane clathrate hydrate. *Journal of Geophysical Research*, *108*(B4), 2182. https://doi.org/10.1029/2002JB001872

Ermakov, A. I., Fu, R. R., Castillo-Rogez, J. C., Raymond, C. A., Park, R. S., Preusker, F., et al. (2017). Constraints on Ceres' internal structure and evolution from its shape and gravity measured by the Dawn spacecraft. *Journal of Geophysical Research: Planets*, *122*, 2267–2293. https://doi.org/10.1002/2017JE005302

Fu, R. R., Ermakov, A. I., Marchi, S., Castillo-Rogez, J. C., Raymond, C. A., Hager, B. H., et al. (2017). The interior structure of Ceres as revealed by surface topography. *Icarus*, *476*, 153–164. https://doi.org/10.1016/j.epsl.2017.07.053

Gault, D. E., & Greeley, R. (1978). Exploratory experiments of impact craters formed in viscous-liquid targets: Analogs for Martian rampart craters? *Icarus*, *34*(3), 486–495. https://doi.org/10.1016/0019-1035(78)90040-4

Hayne, P. O., & Aharonson, O. (2015). Thermal stability of ice on Ceres with rough topography. *Journal of Geophysical Research: Planets*, *120*, 1567–1584. https://doi.org/10.1002/2015JE004887

Heather, D. J., & Dunkin, S. K. (2003). Geology and stratigraphy of King crater, lunar farside. *Icarus*, *163*(2), 307–329. https://doi.org/10.1016/S0019-1035(02)00063-5

Hiesinger, H., Marchi, S., Schmedemann, N., Schenk, P., Pasckert, J. H., Neesemann, A., et al. (2016). Cratering on Ceres: Implications for its crust and evolution. *Science*, *353*(6303), aaf4759. https://doi.org/10.1126/science.aaf4759

Holsapple, K. A. (1993). The scaling of impact processes in planetary sciences. *Annual Review of Earth and Planetary Sciences*, *21*(1), 333–373. https://doi.org/10.1146/annurev.ea.21.050193.002001

Horner, V. M., & Greeley, R. (1982). Pedestal craters on Ganymede. *Icarus*, *51*(3), 549–562. https://doi.org/10.1016/0019-1035(82)90145-2

Howard, K. A., (1972). Ejecta blankets of large craters exemplified by King Crater, Apollo 16 preliminary science report, NASA Spec. Publ. SP-315, pp. 29–70–29-77

Hughson, K. H. G., Russell, C. T., Schmidt, B. E., Travis, B., Preusker, F., Neesemann, A., et al. (2019). Normal faults on Ceres: Insights into the mechanical properties and thermal history of Nar Sulcus. *Geophysical Research Letters*, *46*, 80–88. https://doi.org/10.1029/2018GL080258

Hughson, K. H. G., Russell, C. T., Williams, D. A., Buczkowski, D. L., Mest, S. C., Pasckert, J. H., et al. (2018). The Ac-H-5 (Fejokoo) quadrangle of Ceres: Geologic map and geomorphological evidence for ground ice mediated surface processes. *Icarus*, *316*, 63–83. https://doi.org/10.1016/j.icarus.2017.09.035

Jaumann, R., Clark, R. N., Nimmo, F., Hendrix, A. R., Buratti, B. J., Denk, T., et al. (2009). Icy satellites: Geological evolution and surface processes. In M. K. Doughty, L. W. Esposito, & S. M. Krimigis (Eds.), *Saturn from Cassini-Huygens* (pp. 637–681). Dordrecht: Springer. https://doi.org/10.1007/978-1-4020-9217-6_20

Jia, J., Liang, Y., Tsuji, T., Murata, S., & Matsuoka, T. (2016). Microscopic origin of strain hardening in methane hydrate. *Scientific Reports*, *6*(1), Article number: 23548. https://doi.org/10.1038/srep23548

Jones, E., Caprarelli, G., & Osinski, G. R. (2016). Insights into complex layered ejecta emplacement and subsurface stratigraphy in Chryse Planitia, Mars, through an analysis of THEMIS brightness temperature data. *Journal of Geophysical Research: Planets*, *121*, 986–1015. https://doi.org/10.1002/2015JE004879

Komatsu, G., Ori, G. G., Di Lorenzo, S., Rossi, A. P., & Neukum, G. (2007). Combinations of processes responsible for Martian impact crater "layered ejecta structures" emplacement. *Journal of Geophysical Research*, *112*, E06005. https://doi.org/10.1029/2006JE002787

Kraus, R. G., Senft, L. E., & Stewart, S. T. (2011). Impacts onto H_2O ice: Scaling laws for melting, vaporization, excavation and final crater size. *Icarus*, *214*(2), 724–738. https://doi.org/10.1016/j.icarus.2011.05.016

Li, L., Yue, Z., Di, K., & Peng, M. (2015). Observations of Martian layered ejecta craters and constraints on their formation mechanisms. *Meteoritics and Planetary Science*, *50*(3), 508–522. https://doi.org/10.1111/maps.12438

Marchi, S., Ermakov, A., Raymond, C. A., Fu, R. R., O'Brian, D. P., Bland, M. T., et al. (2016). The missing large impact craters on Ceres. *Nature Communications*, *7*(1), 12,257. https://doi.org/10.1038/ncomms12257

McCord, T. B., & Sotin, C. (2005). Ceres: Evolution and current state. *Journal of Geophysical Research*, *110*, E05009. https://doi.org/10.1029/2004je002244

Melosh, H. J. (1979). Acoustic fluidization: A new geologic process? *Journal of Geophysical Research*, *84*(B13), 7513–7520. https://doi.org/10.1029/JB084iB13p07513

Melosh, H. J. (1989). *Impact cratering: A geologic process*. Oxford University Press: Oxford Monographs on Geology and Geophysics. No. 11

Mouginis-Mark, P. (1979). Martian fluidized crater morphology: Variations with crater size, latitude, altitude, and target material. *Journal of Geophysical Research*, *84*(B14), 8011–8022. https://doi.org/10.1029/JB084iB14p08011

Mouginis-Mark, P. (1981). Ejecta emplacement and modes of formation of Martian fluidized ejecta craters. *Icarus*, *45*(1), 60–76. https://doi.org/10.1016/0019-1035(81)90006-3

Mouginis-Mark, P. J. (1987). Water or ice in the Martian regolith?: Clues from rampart craters seen at very high resolution. *Icarus*, *71*(2), 268–286. https://doi.org/10.1016/0019-1035(87)90152

Mouginis-Mark, P. J., & Baloga, S. M. (2006). Morphology and geometry of the distal ramparts of Martian impact craters. *Meteoritics & Planetary Science*, *41*(10), 1469–1482. https://doi.org/10.1111/j.1945-5100.2006.tb00430.x

Oberbeck, V. R. (1975). The role of ballistic erosion and sedimentation in lunar stratigraphy. *Reviews of Geophysics*, *13*(2), 337–362. https://doi.org/10.1029/RG013i002p00337

Osinski, G. R. (2006). Effect of volatiles and target lithology on the generation and emplacement of impact crater fill and ejecta deposits on Mars. *Meteoritics & Planetary Science*, *41*(10), 1571–1586. https://doi.org/10.1111/j.1945-5100.2006.tb00436.x

Park, R. S., Konopliv, A. S., Bills, B. G., Rambaux, N., Castillo-Rogez, J. C., Raymond, C. A., et al. (2016). A partially differentiated interior for (1) Ceres deduced from its gravity field and shape. *Nature*, *537*(7621), 515–517. https://doi.org/10.1038/nature18955

Parzen, E. (1962). On estimation of a probability density function and mode. *The Annals of Mathematical Statistics*, *33*(3), 1065–1076. https://doi.org/10.1214/aoms/1177704472

Pedregosa, F., Varoquaux, G., Gramfort, A., Michel, V., Thirion, B., Grisel, O., et al. (2011). Scikit-learn: Machine learning in Python. *Journal of Machine Learning Research*, *12*, 2825–2830.

Platz, T., Nathues, A., Sizemore, H. G., Crown, D. A., Hoffmann, M., Schaefer, M., et al. (2018). Geological mapping of the Ac-10 Rongo Quadrangle of Ceres. *Icarus*, *316*, 140–153. https://doi.org/10.1016/j.icarus.2017.08.001

Prettyman, T. H., Yamashita, N., Toplis, M. J., McSween, H. Y., Schorghofer, N., Marchi, S., et al. (2017). Extensive water ice within Ceres' aqueously altered regolith: Evidence from nuclear spectroscopy. *Science*, *355*(6320), 55–59.

Preusker, F., Scholten, F., Matz, K. -D., Elfner, S., Jaumann, R., Roatsch, T. et al. (2016). Dawn at Ceres—Shape model and rotation state. Paper presented at LPSC XLVII, Abs. #1954.

Ramana, Y. V., & Gogte, B. S. (1989). Dependence of coefficient of sliding friction in rocks on lithology and mineral characteristics. *Engineering Geology*, *26*(3), 271–279. https://doi.org/10.1016/0013-7952(89)90014-8

Richardson, J. E., Melosh, H. J., Artemeiva, N. A., & Pierazzo, E. (2005). Impact cratering theory and modeling for the Deep Impact Mission: From mission planning to data analysis. *Space Science Reviews*, *117*(1-2), 241–267. https://doi.org/10.1007/s11214-005-3393-5

Robbins, S. J., Runyon, K., Singer, K. N., Bray, V. J., Beyer, R. A., Schenk, P., et al. (2018). Investigation of Charon's craters with abrupt terminus ejecta, comparisons with other icy bodies, and formation implications. *Journal of Geophysical Research: Planets*, *123*, 20–36. https://doi.org/10.1002/2017JE005287

Rosenblatt, M. (1956). Remarks on some nonparametric estimates of a density function. *The Annals of Mathematical Statistics*, *27*(3), 832–837. https://doi.org/10.1214/aoms/1177728190

Runyon, K. D., & Barnouin, O. S. (2018). Preliminary laboratory investigations of ejecta emplacement dynamics and morphology with planetary applications. *Planetary and Space Science*, *160*, 39–55. https://doi.org/10.1016/j.pss.2018.03.014

Russell, C. T., Raymond, C. A., Ammannito, E., Buczkowski, D. L., De Sanctis, M. C., Hiesinger, H., et al. (2016). Dawn arrives at Ceres: Exploration of a small volatile-rich world. *Science*, *353*(6303), 1008–1010. https://doi.org/10.1126/science.aaf4219

Schenk, P. (2010). Atlas of the Galilean satellites: Ganymede. In *Atlas of the Galilean satellites* (Chap. 5, pp. 32–35). Cambridge, UK: Cambridge University Press. https://doi.org/10.1017/CBO9780511676468.009

Schmidt, B. E., Hughson, K. H. G., Chilton, H. T., Scully, J. E. C., Platz, T., Nsthues, A., et al. (2017). Geomorphological evidence for ground ice on dwarf planet Ceres. *Nature Geoscience*, *10*(5), 338–343. https://doi.org/10.1038/ngeo2936

Schröder, S. E., Maue, T., Gutiérrez Marqués, P., Mottola, S., Aye, K. M., Sierks, H., et al. (2013). In-flight calibration of the Dawn framing camera. *Icarus*, *226*(2), 1304–1317. https://doi.org/10.1016/j.icarus.2013.07.036

Schröder, S. E., Mottola, S., Matz, K. -D., & Roatsch, T. (2014). In-flight calibration of the Dawn framing camera II: Flat fields and stray light correction. *Icarus*, *234*, 99–108. https://doi.org/10.1016/j.icarus.2014.02.018

Schulson, E. M., & Fortt, A. L. (2012). Friction of ice on ice. *Journal of Geophysical Research*, *117*, B12204. https://doi.org/10.1029/2012JB009219

Schultz, P. H. (1992). Atmospheric effects on ejecta emplacement. *Journal of Geophysical Research*, *97*(E7), 11,623–11,662. https://doi.org/10.1029/92JE00613

Schultz, P. H., & Gault, D. E. (1979). Atmospheric effects on Martian ejecta emplacement. *Journal of Geophysical Research*, *84*(B13), 7669–7687. https://doi.org/10.1029/JB084iB13p07669

Senft, L. E., & Stewart, S. T. (2008). Impact crater formation in icy layered terrains on Mars. *Meteoritics & Planetary Science*, *43*(12), 1993–2013. https://doi.org/10.1111/j.1945-5100.2008.tb00657.x

Senft, L. E., & Stewart, S. T. (2011). Modeling the morphological diversity of impact craters icy satellites. *Icarus*, *214*(1), 67–81. https://doi.org/10.1016/j.icarus.2011.04.015

Shoemaker, E. M. (1962). In Z. Kopal (Ed.), *Interpretation of lunar craters. Physics and astronomy of the Moon*, (pp. 283–359). New York: Academic Press.

Sierks, H., Keller, H. U., Jaumann, R., Michalik, H., Behnke, T., Bubenhagen, F., et al. (2011). The Dawn framing camera. *Space Science Reviews*, *163*(1-4), 263–327. https://doi.org/10.1007/s11214-011-9745-4

Silverman, B. W. (1986). *Density estimation for statistics and data analysis*. London: Chapman & Hall. https://doi.org/10.1007/978-1-4899-3324-9

Sizemore, H. G., Schmidt, B. E., Buczkowski, D. A., Sori, M. M., Castillo-Rogez, J. C., Berman, D. C., et al. (2018). A Global Inventory of Ice-Related Morphological Features on Dwarf Planet Ceres: Implications for the evolution and current state of the cryosphere. *Journal of Geophysical Research: Planets*, *123*. https://doi.org/10.1029/2018JE005699

Stewart, S. T., O'Keefe, J. D., Ahrens, T. J. (2001). The relationship between rampart crater morphologies and the amount of subsurface ice. Paper presented at Lunar Planet. Sci. XXXII. Abstract 2090.

Thomas, P. C., Parker, J. M., McFadden, L. A., Russell, C. T., Stern, S. A., Sykes, M. V., & Young, E. F. (2005). Differentiation of the asteroid Ceres as revealed by its shape. *Nature*, *437*(7056), 224–226. https://doi.org/10.1038/nature03938

Wada, K., & Barnouin-Jha, O. S. (2006). The formation of fluidized ejecta on Mars by granular flows. *Meteoritics & Planetary Science*, *41*(10), 1551–1569. https://doi.org/10.1111/j.1945-5100.2006.tb00435.x

Weiss, D. K., & Head, J. W. (2013). Formation of double-layered ejecta craters on Mars: A glacial substrate model. *Geophysical Research Letters*, *40*, 3819–3824. https://doi.org/10.1002/grl.50778

Weiss, D. K., & Head, J. W. (2014). Ejecta mobility of layered ejecta craters on Mars: Assessing the influence of snow and ice deposits. *Icarus*, *233*, 131–146. https://doi.org/10.1016/j.icarus.2014.01.038

Weiss, D. K., & Head, J. W. (2018). Testing landslide and atmospheric-effects models for the formation of double-layered ejecta craters on Mars. *Meteoritics and Planetary Science*, *53*(4), 741–777. https://doi.org/10.1111/maps.12859

Woronow, A. (1981). Preflow stresses in Martian rampart ejecta blankets: A means of estimating the water content. *Icarus*, *45*(2), 320–330. https://doi.org/10.1016/0019-1035(81)90037-3

Zolotov, M. Y. (2009). On the composition and differentiation of Ceres. *Icarus*, *204*(1), 183–193. https://doi.org/10.1016/j.icarus.2009.06.011